Distal ejecta from lunar impacts: Extensive regions of rocky deposits

Joshua L. Bandfield[1], Joshua T.S. Cahill[2], Lynn M. Carter[3], Catherine D. Neish[4], G. Wesley Patterson[2], Jean-Pierre Williams[5], David A. Paige[5]

[1]Space Science Institute
[2]Johns Hopkins University Applied Physics Laboratory
[3]NASA Goddard Space Flight Center
[4]Department of Earth Sciences, The University of Western Ontario
[5]Earth, Planetary, and Space Sciences, University of California, Los Angeles

Manuscript Correspondence:

Joshua Bandfield
Space Science Institute
4750 Walnut Street, Suite 205
Boulder, CO 80301, USA

jbandfield@spacescience.org

Manuscript Pages: 32
Figures: 14
Keywords: Moon, surface; Impact processes; Infrared observations; Radar observations

Abstract

Lunar Reconnaissance Orbiter (LRO) Diviner Radiometer, Mini-RF, and LRO Camera data were used to identify and characterize rocky lunar deposits that appear well separated from any potential source crater. Two regions are described: 1) A ~18,000 km^2 area with elevated rock abundance and extensive melt ponds and veneers near the antipode of Tycho crater (167.5°E, 42.5°N). This region has been identified previously, using radar and imaging data. 2) A much larger and more diffuse region, covering ~730,000 km^2, centered near 310°E, 35°S, containing elevated rock abundance and numerous granular flow deposits on crater walls. The rock distributions in both regions favor certain slope azimuths over others, indicating a directional component to the formation of these deposits. The spatial distribution of rocks are consistent with the arrival of ejecta from the west and northwest at low angles (~10–30°) above the horizon in both regions. The derived age and slope orientations of the deposits indicate that the deposits likely originated as ejecta from the Tycho impact event. Despite their similar origin, the deposits in the two regions show significant differences in the datasets. The Tycho crater antipode deposit covers a smaller area, but the deposits are pervasive and appear to be dominated by impact melts. By contrast, the nearside deposits cover a much larger area and numerous granular flows were triggered. However, the features in this region are less prominent with no evidence for the presence of impact melts. The two regions appear to be surface expressions of a distant impact event that can modify surfaces across wide regions, resulting in a variety of surface morphologies. The Tycho impact event may only be the most recent manifestation of these processes, which likely have played a role in the development of the regolith throughout lunar history.

Highlights

Two regions are identified with rocky surfaces on slopes of preferred orientations

Impact melts and veneers are prevalent throughout the Tycho antipode region

The region on the lunar nearside is dominated by rock fields and granular flows

The deposits in both regions likely originated as ejecta from the Tycho impact event

Distant impacts can modify large swaths of the lunar surface in a variety of ways

1. Introduction

1.1 Previous work

Recent spacecraft measurements have revealed new details about lunar processes that have built on the wealth of information returned from the Apollo and Luna programs. The systematic and global collection of radar, thermal infrared, and high-resolution images by the Lunar Reconnaissance Orbiter (LRO) has provided a new perspective on the nature and variety of lunar surface materials (e.g., *Paige et al.*, 2010; *Robinson et al.*, 2010; *Nozette et al.*, 2010). In particular, impact related processes exhibit a greater diversity than has been previously understood. Impacts and impact generated melts have been characterized at a level of detail that could not be achieved prior to these recent datasets (*Bray et al.*, 2010; *Denevi et al.*, 2012; *Carter et al.*, 2012; *Neish et al.*, 2014; *Stopar et al.*, 2014).

These new datasets have been used to identify an unusual region on the lunar far side, centered near 167.5°E, 42.5°N. Surfaces in this area display numerous features that appear to have formed via flows and ponding. The large-scale morphology of this area appears typical of heavily cratered lunar highlands. However, radar, thermal infrared, and high-resolution imaging measurements display properties that, in some ways, resemble melt ponds and rocky surfaces typically associated with young impact craters (*Robinson et al.*, 2011; 2015; *Carter et al.*, 2012; *Bandfield et al.*, 2013). The surface materials are highly heterogeneous and distributed over a large area ~100–150 km in diameter. In addition, there is no associated source crater of the appropriate size and age nearby.

Robinson et al. (2011; 2015) first described the morphology of these deposits based on LRO Camera (LROC) high-resolution images and associated digital elevation models, focusing on the distinctive features that appear to be melt ponds. These deposits fill local topographic lows and are extremely flat, coinciding with equipotential surfaces. Rough, rocky surfaces and flow features are typically located on slopes adjacent to these ponds. In addition, what appears to be veneers of impact

melts coat the preexisting terrain in a heterogeneous pattern throughout the region. *Robinson et al.* (2015) suggested impact melt as the most likely source of these materials and total melt volume is estimated to be 8 km^3, which would require a source crater >20km in diameter. However, they also noted that the distribution over such a large area in hundreds of discrete occurrences is not typical of impact melts, which tend to form discrete melt ponds and veneers within and adjacent to the source crater (Figure 1).

Carter et al. (2012) also noted the presence of features with radar properties similar to impact melts in this region. Numerous widely distributed ponds and flows display high circular polarization ratio (CPR) values in LRO Mini-RF S-band (12.6 cm wavelength) radar images, consistent with rocky materials. As with the high-resolution visible wavelength images, the Mini-RF data show no sign of a potential source crater nearby. *Carter et al.* (2012) also noted the presence of similar impact melt features without an obvious nearby source near Keeler Crater (157°E, 11°S). In this case, the associated morphological impact melt features appear subdued, perhaps indicating an older formation.

The numerous melt ponds and veneer surfaces near 167.5°E, 42.5°N are distributed across an area that nearly coincides with the antipode of Tycho crater. For slowly rotating bodies, axisymmetric models of ejecta emplacement predict enhanced accumulation of ejected material at the antipode (*Moore et al.*, 1974). In addition, crater-size frequency distributions yield a model age of ~26 Ma for the melt ponds, consistent with a late Copernican formation age (*Robinson et al.*, 2015). This age is consistent with similar analyses of Tycho crater impact melts (22–74 Ma; *Hiesinger et al*., 2012; *Zanetti et al.*, 2015), is too young for Jackson Crater, and is too old for Giordano Bruno (*Robinson et al.*, 2015). Although there are large uncertainties in the derived ages, they are all derived from crater size-frequency distributions of impact melt surfaces. These surfaces presumably have similar crater formation and retention properties that allow for a precise comparison of relative formation age. The similarity in derived age and antipodal location relative to Tycho crater suggests that the Tycho impact

event is the source of the melt ponds. However, the mechanisms required for the emplacement of such large volumes of impact melt at such large distances are not well understood and are contradicted by studies completed prior to the LRO mission (*Robinson et al.*, 2015; e.g., *Hawke and Head*, 1977).

The presence of such a large number of widely distributed impact melt features at such a distance from any potential source is remarkable and unexpected. Although the remote sensing observations have provided significant clues, the specific event and mechanisms of the formation of these features is currently poorly understood.

1.2 Scope of this work

In this work, we use the Diviner Radiometer along with Mini-RF synthetic aperture radar and LROC imaging data to identify and characterize rocky lunar deposits that appear to be well separated from any potential source crater. Our focus here is the exposed rocky surfaces, rather than the melt ponds that are described in detail in *Robinson et al.* (2015) because the melt ponds quickly form a veneer of regolith that hides their rocky signatures in the Diviner data (*Bandfield et al.*, 2011). The source of the rocky materials include solid and perhaps molten ejecta from a distant, large impact.

Although the deposits near the antipode of Tycho crater are the most prominent of these deposits, other potential distal deposits are possible and an additional region on the lunar nearside is also described here. From the perspective of the three LRO datasets, we show that the rocky deposits have a strong dependence on slope orientation and it is possible to estimate incoming trajectories of ejecta material. We also show here that the limited azimuth range of the influx of material places constraints on its origin and is inconsistent with an azimuthally symmetric antipodal focusing of ejecta material. The impact that formed Tycho crater was likely an oblique impact, resulting in a distinct pattern and range of ejecta launch azimuths and elevations. We find that the distribution of the deposits are consistent with the restricted ejecta orientations.

2. Data and methods

2.1 Diviner Radiometer

The Diviner Radiometer has 7 thermal infrared spectral channels; 3 spectral filters are near 8 μm wavelengths and separate filters cover ~13–23, 25–41, 50–100, and 100–400 μm wavelengths (*Paige et al.*, 2010). Each channel consists of a 1 by 21 element detector array and data are collected in a pushbroom configuration. The spatial sampling of Diviner is ~160 by 320 m from a 50 km polar orbit. The local time of Diviner observations migrated across the full diurnal cycle throughout the primary LRO mission. The orbit was changed to ~40 by 170 km for the LRO Extended Science Mission starting in 2011 (*Keller et al.*, 2015). More complete descriptions of the Diviner instrument characteristics and operations are given in *Paige et al.* (2010).

The data used for the analysis of individual craters were derived from the Level 2 Gridded Data Products available at the Planetary Data System (*Paige et al.*, 2011). These data are constructed from the calibrated Diviner Reduced Data Record (RDR) and resampled to 128 pixels per degree (ppd). The true resolution of the data is variable and can be lower by a factor of 2–3 because of the high spacecraft altitudes in the elliptical orbit during the Extended Science Mission.

We used data collected from Diviner channels 6–8 (with full width half maximum bandpasses of 13–23, 25–41, and 50–100 μm respectively) acquired between July 5, 2009 and September 2, 2012, as well as gridded maps of the local time of each observation. Each of the maps covers a single lunar cycle (~28 days), resulting in 46 separate maps. Each pixel of each map essentially corresponds to a single location and acquisition time, though it may represent an areally weighted average of measurements acquired by several detectors (*Williams et al.*, 2015).

These data were used to produce updated rock abundance and rock-free regolith temperature data products that were derived using the methods described in *Bandfield et al.* (2011). Because lunar rocks are typically much warmer than the surrounding regolith during the lunar night, mixed surfaces with

both rocks and regolith will contribute variable amounts to the measured radiance at the different measured wavelengths. For the algorithm used here, rock temperatures are modeled *a priori* using the properties for vesicular basalt described by *Horai and Simmons* (1972) and the 1-dimensional thermal model described by *Vasavada et al.* (1999). Diviner measured radiance at three wavelengths (channels 6–8) is then fit using a non-linear least-squares algorithm with rock fraction and rock-free regolith temperature as the free parameters used for the optimization. Data were restricted to local times of 1930–0530 H to avoid anisothermality effects due to solar heating and shading on sub-pixel local slopes.

Rock concentrations retrieved from this technique represent the areal coverage of ~1 m diameter rocks from 0–1 (0–100%). This technique is not sensitive to smaller rock sizes, and coverage of smaller rock size fractions is predicted to be much higher (*Cintala and McBride*, 1995). For example, typical scaling relationships indicate that a surface with 10% areal coverage of ≥1 m diameter rocks would be nearly completely covered with rocks ≥0.1 m. The ~1 m rock size sensitivity of the Diviner data falls between that of LROC (~2–3 m) and Mini-RF S-band (~0.1 m) data.

Several improvements were made to the rock abundance retrieval algorithm used here over that described by *Bandfield et al.* (2011). First, we accounted for regional slopes to predict the modeled rock temperatures using the LROC global digital terrain model (DTM) sampled at 128 ppd (*Scholten et al.*, 2012). The slope and slope azimuth at each location was used to adjust the apparent local time and latitude of the modeled rock temperatures for each measurement. For example, a rock at the equator on a 10° south-facing slope would be modeled using rock temperatures for 10°S.

This approximation for local slopes results in an improvement in the retrieved rock abundance and rock-free regolith temperature values of *Bandfield et al.* (2011). The previous data products showed systematic errors of 0.1–0.2% in rock abundance values that were highly correlated with surface slopes. In general, equatorward-facing slopes had slightly elevated rock abundance values relative to

poleward-facing slopes, because the rock temperatures were under- and overestimated for equator and pole-facing slopes respectively. These systematic errors are no longer present after accounting for the local slopes in the rock temperature modeling. This improvement in the data reduces the uncertainty in the results presented here, particularly because of our focus on rock distributions with respect to surface slopes.

In addition the rock abundance and regolith temperature data products were extended to 80°N/S latitude, though these high latitude data are not used in the work described here. No retrieval is performed where the local slope exceeds the equivalent of 80° latitude. For example, a 10° north-facing slope at 75°N does not meet the necessary criteria and no rock abundance value would be retrieved at this location.

2.2 Mini-RF Radar

We included Mini-RF radar data to support the Diviner observations. Mini-RF is a synthetic aperture radar utilizing X-band and S-band frequencies (~4.2 and 12.6 cm wavelengths respectively) at 15 and 75 m sampling (*Nozette et al.*, 2010). We used the S-band total power (S1), circular polarization ratio (CPR), and M-chi decomposition (*Raney et al.*, 2012; *Cahill et al.*, 2014) data products to identify both flow and melt pond features.

Total power (Stokes parameter S1) images were used to identify melt features using Mini-RF data. Although these images are heavily influenced by topography, they also contain less noise, allowing for easier identification of less prominent features. CPR is a dimensionless parameter that is the ratio of the same sense circularly polarized return (S1 – S4) to the opposite sense circularly polarized return (S1 + S4). This parameter is highly sensitive to scatterers (such as rocks) of roughly the same size as the wavelength of the signal (e.g., *Campbell et al.*, 2010). In addition, M-chi decomposition images were used to help distinguish the type and source of radar scattering objects (*Raney et al.*, 2012). The M-chi decomposition separates the returned radar signal into three parameters: odd and even-bounce polarized

signatures and depolarized signatures (*Raney et al.*, 2012). These different radar return signatures are sensitive to different aspects of the lunar surface and subsurface. For example, the odd bounce image represents the strength of the polarized return that has reflected off a single surface or subsurface (or any odd number of surfaces). Most commonly, a strong odd-bounce signal represents either surface scattering or layering present between materials of different properties. By contrast, the double bounce polarized signal represents the strength of the polarized return that has reflected off of two (or any even number) surfaces. A typical example with rocky surfaces occurs when the transmitted radar signal is bounced off natural corner reflectors, such as the ground and the face of a rock before returning back to the receiver. This type of signal can also result from interaction of multiple interfaces within the subsurface, such as rocks within a regolith matrix. Lastly, the depolarized signal image primarily represents volume scattering. This is sensitive to heterogeneities (such as rocks within a fine regolith matrix) within the upper ~1–2 m of lunar regolith.

The Mini-RF S-band data are sensitive to the presence of rocks and heterogeneous materials in the upper ~1–2 m of regolith, depending on its dialectric properties (e.g., *Carter et al.*, 2012; *Neish et al.*, 2014; *Cahill et al.*, 2014). This allows for the detection of melt flows and pond features, even if buried in the shallow sub-surface. This data complements the Diviner data, which is only sensitive to rocks at or within a few centimeters of the surface. It has been shown that rocky materials persist in the lunar subsurface after a regolith covering quickly develops on the surface, masking their thermophysical signature (*Bandfield et al.*, 2011; *Ghent et al.*, 2014; *Neish et al.*, 2014).

2.3 LRO Camera

We also used LROC data for this study, including both wide and narrow angle camera datasets. As described in Section 2.1 , elevation derived from the LROC Wide Angle Camera (WAC) was used to determine the slope and azimuth of surfaces to model rock temperatures. Details of the generation of elevation data are provided in *Scholten et al.* (2012). The elevation data was also used to identify

correlations between the rock abundance and the slope and azimuth of surfaces.

LROC Narrow Angle Camera (NAC) images were used to identify meter-scale surface morphologies and textures associated with distinct surfaces identified in the Diviner rock abundance data. We focus here on the relationship between the high resolution images and the thermophysical properties. A more detailed study with a focus on morphological characteristics, crater densities, and other features identified in LROC NAC images near the antipode of Tycho crater is described in *Robinson et al.* (2015).

3. Results

3.1 Tycho antipodal region rock distributions

Elevated rock concentrations are present within an irregular area roughly 150 km in diameter, covering ~12,000 km^2, and centered near 167.5°E, 42.5°N (Figure 2). Outside this region, surfaces are largely free of rocks, with areal coverages typically ~0.2–0.3% and rarely exceeding 1%. We use the terms "areal abundance" and "concentration" interchangeably here and express the surface coverage of rocks in terms of percentage (i.e., 10 m^2 rock coverage within a total surface area of 100 m^2 is described as 10% rock areal abundance). Within the region of 164–170°E, 40–46°N (encompassing the surfaces with anomalous rock concentrations), the maximum rock areal coverage is 29.7%, though few surfaces exceed 8%. The total area with elevated rock concentrations (≥1%) is 5121 km^2. The region of elevated rock concentrations lacks a distinct boundary, and the transition to typical background rock concentrations can be diffuse. However, this boundary appears relatively sharp along its southern margin (Figure 2).

The spatial distribution of rocky surfaces is highly variable within this region, with many contiguous areas ~1–10 km across either having elevated rock concentrations or being similar to typical low rock concentration lunar highlands surfaces. There also appears to be two distinct regions

separated by a wedge of low rock concentration surfaces towards the northwest (Figure 2).

Elevated rock concentrations occur on both level and sloped surfaces and both within and outside craters. Within craters, elevated rock concentrations occur on both the crater walls and floor. However, elevated rock concentrations are highly asymmetrical with regards to the azimuth orientation of the crater wall. This slope azimuth asymmetry appears to be common and is not restricted to an isolated group of craters.

We defined two regions of interest within the area antipodal to Tycho to better illustrate and quantify the asymmetry in rock concentrations on slopes of particular azimuths (Figures 2 and 3). These regions each appear to have high rock concentrations favoring a distinct and limited range of slope azimuths. The regions were separated by visual inspection of the relationship between rock abundance and slope azimuth within local craters and depressions. Although the regions of interest are defined subjectively, together they encompass the full area containing elevated rock concentrations. We also assumed that the two regions are geographically exclusive. Despite the somewhat arbitrary definition of the extent of these two regions, it enables quantification of the relationship between slope azimuth orientations relative to rock concentrations.

Within each region, slopes with elevated rock concentrations are prevalent on both shallow and steep slopes, but are concentrated within a limited range of azimuth angles (Figure 3). The majority of sloped surfaces (slopes >15°) with azimuth orientations towards the west have elevated rock concentrations of (Table 1). Similar patterns are present in the southern region of interest (Figure 3). In this case, the majority of sloped surfaces with azimuth orientations to the north have elevated rock concentrations of (Table 1). To summarize, within the northern region, rocky surfaces dominate west-facing slopes and rocks are largely absent from east-facing slopes. Within the southern region, rocky surfaces dominate northwest-facing slopes and are absent from southeast-facing slopes.

We observe similar orientation patterns within each region of interest by isolating rock distributions

on slopes protected from debris falling from a restricted azimuth and elevation angle. In this case, we assume material is impacting the lunar surface. Slopes where the angle between the direction of falling debris and the vector normal to the local slope is greater than 90° will be protected. For example, debris falling from the north at an elevation of 9° above the horizon cannot impact a south facing surface with a slope of 10°. If the falling debris is the source of rocks in the region, then the protected surfaces should be free of rocks. Because of the significant computational requirements, this simplified model only takes the local slope into account and does not consider "cast shadows". For example, a level surface adjacent to a steep slope may be in reality protected from incoming material, but would not be considered by the model to be protected. However, as a check on the validity of this assumption, we have included a ray-tracing model that does account for these cast shadows. We found that (as would be expected) the ray-tracing model includes a greater proportion of protected surfaces for a given elevation angle.

Rock concentration distributions were calculated for surfaces protected from falling debris every 5° of azimuth and 2° of elevation from 0–30° above the horizon (Figure 4). In the northern region, the greatest proportion of rock-free surfaces would be protected from debris traveling to the east and southeast for elevations of 0–20° above the horizon (Table 1). In the southern region, rock-free surfaces would be protected from incoming debris traveling to the southeast for elevations of 0–20° above the horizon (Table 1). The modeled protected surfaces from other azimuth angles show a poor match to the data. At these other azimuth angles, many existing rocky surfaces would be shielded from the modeled incoming debris and many rock-free surfaces would not (Figure 4).

There is also a strong dependence of protected surface rock abundance distributions on the elevation angle of incoming debris. At higher angles above the horizon, only the steepest slopes remain protected. As a result, above elevation angles of ~20°, few surfaces would remain protected from incoming material. The fractions of rock-free and rocky protected surfaces becomes more extreme

(both high and low) as the elevation angle of incoming material is increased. There is no apparent peak or plateau with respect to elevation angle (Figure 4).

We mapped the distribution of protected surfaces for various incoming debris azimuth/elevation combinations (Figures 4 and 5). These maps, which include the "cast shadow" ray-tracing model, show that a greater proportion of rock-free surfaces are protected relative to rocky surfaces at higher elevation angles. However, there are also large swaths of rock-free surfaces that would not be protected. At lower elevation angles, more rock-free surfaces are protected, but small rocky areas are also included within the protected areas. Although the correlation is not perfect, the maps show numerous local protected surfaces that largely coincide with rock-free surfaces for certain azimuth and elevation combinations (Figure 5).

As noted by *Robinson et al.* (2015), there are several distinctive surface textures and morphologies present in the region, including several that appear spatially correlated with areas of elevated rock concentrations. As an example, we investigated surfaces within and near a ~10 km diameter crater in this region, centered near 41.95°N and 167.85°E (Designated by the white circle in Figure 6; Figure 7). This crater is located within the southern region of interest, discussed in Section 3.1 , and shows a distinct variation in rock concentration with respect to slope azimuth (Figure 6). North and west facing slopes have elevated rock concentrations, and east and south facing slopes are nearly rock-free. This is consistent with the dependence of rock concentrations on slope orientations throughout the southern region of interest.

Areas with elevated rock concentrations have surfaces that are highly fractured and interspersed with relatively smooth surfaces. The fractures typically run perpendicular to the downslope direction and are spaced several meters apart (Figure 7). Dense fracture networks appear to grade into areas dominated by individual blocks on the surface. These textures commonly appear on sloped surfaces. Near the floor of the crater, surfaces appear smooth and fractures are much less common. Sinuous

rubble piles (about 10–40 m in width and up to ~2 km long) are present that break the relatively rock-free smooth surfaces into separate sections (Figure 7). Other smooth surfaces that are present in local topographic depressions (interpreted by *Robinson et al.*, 2015 as melt ponds) appear to be relatively free of rocks (Figures 1 and 7). Additional rock-free areas have textures similar to typical lunar highlands surfaces (Figure 7).

3.2 Nearside region rocky deposits

3.2.1 Rock distributions

We searched for other regions of elevated rock concentrations with properties similar to those located near the antipode of Tycho crater. Most rocky surfaces are clearly associated with adjacent craters or rilles and are especially prevalent within maria (e.g., *Bandfield et al.*, 2011). However, we identified one region, centered near 310°E, 35°S, that appears to have elevated rock concentrations with some properties similar to the rock distributions found near the Tycho crater antipode (Figure 8).

The region of elevated rock concentrations covers ~730,000 km^2, and is diffuse with no clear boundary. Several relatively smooth mare and cryptomare areas are present within the region. These areas have numerous small craters with elevated rock concentrations, similar to other mare surfaces across the Moon. Other rocky surfaces are present in the region, appearing on slopes within highlands terrain. Outside of fresh craters, elevated rock concentrations are rare within the lunar highlands, and these rocky slopes are not common elsewhere on the Moon.

The rocky highlands surfaces in this region are present on slopes with a preferential orientation. In order to better quantify these trends we defined several regions of interest in a manner similar to our analysis of the Tycho antipode region (Figures 8 and 9). In this case, we defined three regions of interest, but combined the analysis of data because all three regions appear to show similar trends. As discussed in Section 3.1 , the boundaries of the regions of interest are somewhat arbitrary. In this case, the diffuse nature of the region and the presence of more typically rocky mare surfaces make a precise

spatial definition of this anomalous region impossible. Instead, our three regions of interest encompass rocky surfaces within highlands terrain that show strong orientation patterns based on visual inspection.

West and northwest-facing slopes tend to have elevated rock concentrations relative to east-facing slopes (Figure 9). In this case the asymmetrical distribution is not nearly as pronounced as with the Tycho crater antipode deposits, but the trend is still clear. In this case, the majority of surfaces of any azimuth with slopes >15° have low rock concentrations. However, 43% of slopes facing west and northwest have elevated rock concentrations of, compared to only 18% of slopes facing north, east, and south (Table 1).

As before, we also observe similar orientation patterns within the regions of interest by isolating rock distributions on slopes protected from debris falling from a restricted azimuth and elevation angle (Figure 9). In this region, >80% of rock-free surfaces would be protected from debris incoming towards the east and southeast and elevations of 0–20° (Table 1). The fraction of rock-free protected surfaces becomes more extreme (both high and low) as the elevation angle is increased (Figure 9). Again, although the asymmetrical distribution is clearly present, it is not as pronounced as with the Tycho crater antipode deposits.

High-resolution images show surface morphologies distinct from those present at the antipode of Tycho crater. Rock-free surfaces appear to have textures similar to typical lunar highlands surfaces. Melt ponds, indicated by level surfaces filling local topographic depressions, and melt veneers appear to be absent. Rocky surfaces are present on slopes of preferential slope orientations, similar to those present at the antipode of Tycho crater. However, these surfaces lack the fractured textures and flow features present at the Tycho crater antipode site (Figure 10). Instead, boulders of various sizes are present that have a diffuse boundary with rock-free areas. These rocky surfaces also have a higher albedo compared with surrounding rock-free areas.

3.2.2 Granular Flows

Within the larger nearside region, granular flow features are common on crater walls (Figures 11 and 12). Granular flows are clast-supported, where grain-to-grain collisions result in a fluid-like behavior of the bulk material. These features commonly exhibit multiple lobes, levies, and central channels, similar to granular flows identified elsewhere on the lunar surface (e.g., *Xiao et al.,* 2013). Five hundred and twenty individual LROC-NAC images were inspected within this region, with an emphasis on images that covered surfaces of elevated rock abundances. We identified 74 individual craters and one non-crater surface with flow features (Figure 8). High-resolution image coverage (especially with favorable illumination conditions) is not complete within the region, and there are likely additional unidentified granular flows present.

Most craters with granular flow features also exhibit rock fields on the crater walls and rim. However, these craters are typically degraded otherwise and do not show signs of recent slumping, melt ponds within or outside the craters, or rocky ejecta immediately outside the crater (Figure 11). The flow features are common on north, east, and west-facing walls of the crater. Flows on south-facing crater walls are rare and were only identified in one instance, though the illumination conditions make identification of flow features on south-facing slopes more difficult. No flow features were identified on the outside rim of craters, and were only identified on steep slopes.

3.3 Mini-RF

Mini-RF total power (Stokes parameter S1) images were examined for areas covering the Tycho crater antipode and nearside regions (Figure 13). In the Tycho antipode region, surfaces with elevated rock abundances also show elevated backscatter in the radar images. The Tycho antipode region radar images also show numerous bright spots that coincide with melt ponds identified in LROC images. In addition linear patterns of enhanced radar return are present and typically follow a path consistent with downslope flow of molten material. The radar images in this region show a relatively complex pattern

that coincides with the rocky surfaces identified using the Diviner data, along with the flow features and melt ponds identified in LROC images.

By contrast, radar data in the nearside region is highly correlated with rock abundance data (though the S1 radar images also show the expected variations due to slopes facing toward or away from the spacecraft). Both granular flows and the numerous rocky surfaces show similar spatial patterns and can be identified in Diviner, LROC, and Mini-RF datasets. The linear patterns and numerous melt pond features are absent from the radar images in this region. M-chi decomposition data shows an enhanced return signal from all three components where there are blocks present on the surface (Figure 14). This implies that ~0.1 m diameter blocks are only present in the near-subsurface where they are also present at the surface.

4. Discussion

4.1 Tycho antipode deposit formation processes

Robinson et al. (2015) discuss the potential processes that are related to the formation of the numerous and widely distributed impact melts at the antipode of Tycho crater. Based on the absolute model ages derived for the melt deposits and the lack of a viable alternate formation mechanism, the Tycho impact event was ruled the most likely cause of the antipodal deposits (*Robinson et al.*, 2015). Some questions remain, however; for instance, it may be difficult to keep material molten during the minimum several hours it takes to travel from the impact location to the antipode (*Artemieva*, 2013; *Robinson et al.*, 2015). Regardless, meter-sized spheres of material could remain partially molten during travel time or the conversion of kinetic energy to heat on impact at the antipode are viable mechanisms to deliver or produce molten material to the antipode (*Artemieva*, 2013; *Robinson et al.*, 2015; *Jögi and Paige*, 2014).

The rock distributions in the Tycho antipode region clearly favor certain slope azimuths over others.

Even within individual craters, certain slopes are dominated by rubble piles and melt sheets, with melt ponds on the crater floor, while other slopes within the same crater appear untouched and indistinguishable from typical lunar highlands surfaces (Figures 6 and 7). The persistence of this orientation pattern within the two regions (described in Section 3.1) indicates that there is a directional component to the formation of these deposits and that the material primarily arrived from the west and the northwest for the northern and southern regions respectively (Figures 3 and 4). It is of course possible that the regions could be further subdivided or small amounts of incoming material arrived from any azimuth orientation. In addition, the two regions we selected may not be entirely exclusive and there is likely at least some overlap between them. Regardless of these details, the data indicate the presence of material that impacted the surface from at least two dominant directions and incoming material from other directions was much less prevalent.

In addition, the presence of rock-free "shadows" on slopes of certain orientations can be used to constrain the elevation above the horizon for incoming material. At increasing elevation angles, steeper slopes are required to be shielded from incoming material. The rock abundance distributions show that almost all rock-free surfaces in the Tycho crater antipode region would be protected from material arriving primarily from the west and northwest for the north and south regions respectively (Figure 4). In both cases, the material must have arrived from a shallow angle, roughly 10-20° above the horizon. At a higher incoming angle, few slopes would be protected and it is not likely that the many rock-free surfaces observed in the region would still be present. Conversely, at a shallower incoming angle, many surfaces that currently have high rock abundance values would have been protected.

The elevation and azimuth constraints of the incoming material constrain conditions of the source impact. Suborbital material will land at the same elevation angle from which it is launched, so the source impact of the Tycho antipode deposits must have ejected a significant amount of material near 10-20° above the horizon. This shallow angle is unusual except in the instance of oblique impacts (e.g.,

Anderson et al., 2003), such as that which created Tycho crater (e.g., *Schultz et al.*, 1976).

In addition, the azimuth orientation of the Tycho antipode rocky surfaces indicates that material must have been launched towards the east and southeast for the northern and southern regions respectively. The two Tycho antipode deposit regions are nearly identical and nearly overlap, but arrived from these two primary directions. The unique nature of the deposits and surface features in the region, along with their similar age, make it difficult to invoke two separate events to have occurred in recent lunar history to form the deposits. A single impact event near the antipode of the deposits is necessary to produce debris on slopes of two preferential orientations.

In summary, we conclude that the Tycho antipode deposits did indeed form from ejecta from the Tycho impact event. This is based on the following lines of evidence:

- The coincidence of the age of the associated melt ponds with that of Tycho crater (*Robinson et al.*, 2015)
- The two preferential orientations of the deposits at nearly the same location could only have an antipodal source (i.e., Tycho crater)
- The deposit orientations also indicate that the source was an oblique impact towards the east, consistent with the Tycho impact event

Although we are confident that the source of the deposits is the Tycho impact event, we do not understand the reason for their presence at the antipode. There have been many studies that model and document increased ejecta at the antipodal focus of an impact (gravitational focusing), especially for slowly rotating bodies, such as the Moon (e.g., *Moore et al.*, 1974; *Argyle*, 1989; *Kring and Durda*, 2002; *Hood and Artemieva*, 2008). However, the mechanism for this focusing is the intersection of great circles at the impact antipode, allowing for incoming ejecta from a wide range of azimuths. This is not the case for the Tycho antipode deposits, which arrived from two dominant azimuth and elevation angles. As shown in Figure 4, it is possible that nearly all of the rocky material could have arrived from

only these two azimuth and elevation angles.

Although gravitational focusing is also likely to have occurred, its influence at the antipode of Tycho crater does not appear to be significant. Where rock-free "shadows" are present, the surface appears entirely untouched by this event and indistinguishable from typical lunar surfaces. It is possible (and indeed probable; *Jögi and Paige*, 2015) that an oblique impact, such as that which formed Tycho crater, will result in a azimuthally asymmetric pattern of impact directions at the antipodal focus. However, this mechanism still relies on a high concentration of incoming material from a substantial range of azimuth orientations to distinguish the antipode from other lunar surfaces.

Gravitational focusing relies on the confluence of great circles to concentrate material near the antipode of an impact crater. What we identify and describe here is instead consistent with concentrations of ejecta launched at a limited number and range of elevations, azimuths and velocities. As such, the underlying process responsible for the rocky deposits that we find at the antipode of Tycho crater does not require the deposits to be at that particular location. The restricted range of directions of incoming material appears to be as valid if the two rocky regions were located at any other set of locations on the Moon, if the preferential ejecta launch velocities or angles happened to be different.

It may be that the presence of these ejecta at the antipode is a coincidence. For example, a higher launch velocity would have separated and placed the two regions of rocky materials and melts further east and southeast, for the north and south regions respectively. Conversely, a lower launch velocity would have placed the materials to the west and northwest of their current location. We do not know of any mechanism that launches ejecta at a specific and narrow range of velocities just sufficient to reach the antipode. Consequently, although we believe the evidence is strong that the Tycho impact event is the source of the deposits at its antipode, we also believe that their presence at the antipode may simply be an unusual and distracting coincidence. There is, however, some evidence for similar deposits near the antipode of Copernicus crater (discussed in Section 4.3).

4.2 Nearside deposit formation processes

There are two types of rocky surface morphologies associated with the nearside deposits; 1) the widespread occurrence of numerous isolated rubble piles, and 2) granular flow deposits on crater walls. High-resolution images do not show evidence for directionality to the deposits (e.g., a “smearing out” in the direction of impact). As with the Tycho crater antipode deposits, there is little in the high-resolution images that clearly indicates the impact of the material on the surface, such as secondary craters, or gouging that may be expected by low-velocity and low elevation angle impacts. However, it is not clear that a widely distributed collection of small objects impacting at low elevation angles and velocities would necessarily produce surface features beyond rubble piles.

The numerous granular flows are in the same region as the rubble piles, but only occur on crater walls. This is likely because few other surfaces in the region are steep enough to sustain granular flows. The presence of granular flows on crater walls is not unusual on the Moon. However, their presence on 74 separate craters, many of which are old and degraded, is unique. It appears likely that the same incoming material that formed rubble piles throughout the region also caused the granular flows. Although the process of triggering granular flows on slopes composed of unconsolidated materials is intuitive, some of the details remain unclear. For example, it is not known what proportions of the granular flows are composed of the incoming material or the preexisting regolith. In many cases, the craters are old and degraded and both the radar data and the lack of excavated blocks near small recent craters show that rocky materials are not present within a few meters of the surface. Consequently, either the granular flows are composed of mixtures of incoming rocky material and fine-particulate regolith, or the impacting material excavated more deep-seated rocky material that was incorporated into the granular flows.

Neither radar or visible images show evidence for the presence of any melt associated with the nearside deposits. There are no linear features in either dataset that indicate downslope flow, no cooling

cracks or veneers, and no flat surfaces within local depressions. The radar data in particular shows a large contrast in the character of the Tycho antipode and nearside deposits. No small, rounded melt ponds or possible melt flows are observed in this region (Figures 13 and 14).

The nearside rocky deposits and granular flows show orientation patterns that are similar to the Tycho crater antipode deposits (Figure 9). However, the nearside deposits show a less pronounced orientation effect, are typically much more diffuse and subtle, and cover a much larger area. There are surfaces with high rock abundances, such as rocky craters, showing the presence of rocks on all slope azimuths with no orientation effect. It is likely that these rocky surfaces are simply young craters that formed independently of the anomalous rocky surfaces present throughout the region. These other processes that form rocky surfaces make it difficult to completely isolate the anomalous surfaces from what may be considered background lunar rocky surfaces.

The orientation effects in the nearside deposits are clearly present, despite this interference. This is indicated at the local scale with the granular flow deposits and at the larger regional scale with the more non-descript rocky regions. As with the Tycho antipode deposits, the data are consistent with incoming material from the west or northwest. In this case, however, it is likely that the elevation angle of incoming material was higher above the horizon; perhaps 20–30° in this case, compared with 10–20° for the Tycho antipode deposits (Figure 9). Although it is difficult to derive precise elevation angles, the less pronounced rock shadowing effect in the nearside deposits supports a higher elevation angle for incoming material. This elevation angle is still low enough to be consistent with oblique impact launch angles.

There are several possible sources for the nearside rocky deposits and granular flows. Unfortunately, there are no melt ponds present that provide surfaces that can be used for crater counts and derived ages. However, the presence of the rocks in high abundances on the surface indicate that the surfaces are young and probably Copernican in age (e.g., *Bandfield et al.*, 2011; *Ghent et al.*, 2014).

This restricts the potential source to a young impact that occurred somewhere to the west or northwest. Unfortunately, great circles that encompass these incoming directions allow for the source impact to be located at a wide range of locations on the Moon, including recent craters, such as King, Giordano Bruno, Copernicus, Aristarchus, and Tycho.

The relatively low elevation angle and azimuth orientation of incoming material is consistent with an oblique impact towards the east or southeast. This is once again consistent with the Tycho impact event, which would have ejected a significant amount of material at low elevation angles to the east. Although Tycho crater is only ~1000 km to the east of the nearside rocky deposits, the material would have traveled nearly the entire circumference of the Moon in order to impact the surface from the west/northwest.

The longer travel time and widely dispersed nature of the nearside highlands deposits may account for the lack of evidence for melt at this location. A longer travel time would allow molten particles to cool and solidify more completely before impacting the surface. In addition, the dispersed nature of the deposits would make the cumulative heating from the continuous impacts of material, as well as the radiative insulating properties of the material, less efficient as it is traveling through space (*Robinson et al.*, 2015; Jögi and Paige, 2014).

4.3 Other regions with similar properties

No other region on the Moon matches the distinct and extensive nature of the Tycho crater antipode and nearside highlands deposits. However, several areas show morphological similarities that have been identified in high resolution visible wavelength and radar images. One location in particular was identified by *Carter et al.* (2012) near Keeler crater. This region shows what appear to be melt ponds as well as downslope melt flow features. These features bear a distinct similarity to the features identified near the antipode of Tycho crater, although they are not as widespread or prominent. In contrast with the Tycho crater antipode and nearside deposits described here, the Keeler crater features are not

associated with anomalous rock abundance values.

The Keeler crater features are located near the antipode of Copernicus Crater, which is suggestive of a causal relationship. The more subtle and rock-free nature of the deposits is consistent with an older source, such as would be the case for Copernicus (e.g., *Neukum and Koenig*, 1976; *Bogard et al.*, 1994; *Hiesinger et al.*, 2012). However, there is no directional information, such as is present for the Tycho crater antipode and nearside deposits, that provides information about source impact conditions. As such, only its likely older age and presence at the antipode ties the Keeler crater features to the Copernicus impact event.

4.4 Implications for the development of lunar surfaces

Regardless of the source of the rocky deposits described here, it appears that recent, moderate sized lunar impact events can have a large effect on the surface properties of wide regions at a distance far removed from the impact source. In some ways, this is unsurprising and we only need to observe the rays of Tycho and Giordano Bruno craters to understand the widespread effects of impacts on the Moon (e.g., *Wells et al.*, 2010; *Neish et al.*, 2013). However, the surface features and deposits described here appear to be a separate manifestation of the impact process. In this case, large amounts of material are ejected from the impact site within a restricted range of velocities and directions. This bears some similarity to strewn fields, where increased concentrations of tektites are present at large distances from their source crater (e.g., *Glass et al.*, 1979). The enormous volume of material required to form the deposits is larger than anything previously recognized as a strewn field.

Regardless of how the Tycho crater antipode and nearside deposits are classified, or which impacts are responsible for their formation, they show a range of violent and active processes that are likely to have been present throughout lunar history. Their presence supports the notion that granular flows, impact melt features, and rubble piles may be related to distant impact events.

If the source of the deposits is indeed the Tycho impact event, the global effect is even greater than

previously recognized. Although the diameter of Tycho crater is only ~85 km, covering ~5800 km^2, it appears to have modified surface materials in several distant regions covering ~750,000 km^2. This process may be common throughout lunar history and, if so, it must play a large role in the development of the lunar regolith. Even so, the lack of similar deposits in other locations on the Moon suggests that these surface features degrade with time and may only be preserved at depth where rocky materials are protected from micrometeorite breakdown. The presence of similar melt features near Keeler crater may be an older example of this process where surface rocks have been broken down and features are only subtly present in radar and visible imaging datasets.

5. Conclusions

The rocky materials in the two regions described here are the distant surface expressions of a recent lunar impact or impacts. The deposits show distinct orientation effects that indicate they came from low elevation angles above the horizon and primarily from the west and northwest, consistent with an oblique impact to the east or southeast. The directionality and impact angle of these deposits, along with age dating of impact melt ponds by *Robinson et al.* (2015) strongly support the Tycho impact event as the source for the deposits in both regions.

The deposits show a variety of surface morphologies, including granular flows, rubble piles, and melt flows and ponds. These features cover large areas well-separated from the source crater and, without taking a global context into account, would otherwise appear unrelated to their source impact. The effects of impact events appear to be extensive and widespread, leaving surface expressions both detached and covering vast areas relative to the size of the source crater. The Tycho impact event may only be the most recent and visible manifestation of these processes, which likely have played a significant role in the development of the lunar regolith.

Acknowledgments

We would like to thank the LRO, LROC, Mini-RF, and Diviner operations teams for the collection of high quality datasets used in this work. We would also like to thank Sam Lawrence and Julie Stopar for helpful discussions. The Lunar Reconnaissance Orbiter program provided support for this work. We also thank two anonymous reviewers, who provided helpful and constructive comments that significantly improved this manuscript.

References

Anderson, J. L. B., P. H. Schultz, and J. T. Heineck (2003) Asymmetry of ejecta flow during oblique impacts using three-dimensional particle image velocimetry. *J. Geophys. Res.*, *108*, 509410.1029/2003JE002075.

Argyle, E. (1989) The global fallout signature of the K-T bolide impact. *Icarus*, *77*, 220-222 10.1016/0019-1035(89)90018-3

Artemieva, N. (2013) Tycho Crater Ejecta. *Lunar Planet. Sci. Conf.*, *44*, 1413.

Bandfield, J. L., J. T. S. Cahill, L. M. Carter, B. T. Greenhagen, C. D. Neish, G. W. Patterson, N. E. Petro, and D. A. Paige (2013) A Highly Unusual Series of Young Impact Melts and Rocky Surfaces Antipodal to Tycho Crater. *Lunar Planet. Sci. Conf.*, *44*, 1770.

Bandfield, J. L., et al. Lunar surface rock abundance and regolith fines temperatures derived from LRO Diviner Radiometer data. *J. Geophys. Res.*, *116*, 010.1029/2011JE003866 (2011).

Bogard, D. D., D. H. Garrison, C. Y. Shih, and L. E. Nyquist (1994) ^{39}Ar-^{40}Ar dating of two lunar granites: The age of Copernicus. *Geochim. Cosmochim. Acta*, *58*, 3093-3100 10.1016/0016-7037(94)90181-3.

Bray, V. J., L. L. Tornabene, L. P. Keszthelyi, A. S. McEwen, B. R. Hawke, T. A. Giguere, S. A. Kattenhorn, W. B. Garry, B. Rizk, C. M. Caudill, L. R. Gaddis, and C. H. van der Bogert (2010) New insight into lunar impact melt mobility from the LRO camera. *Geophys. Res. Lett.*, *37*, L2120210.1029/2010GL044666.

Cahill, J. T. S., B. J. Thomson, G. W. Patterson, D. B. J. Bussey, C. D. Neish, N. R. Lopez, F. S. Turner, T. Aldridge, M. McAdam, H. M. Meyer, R. K. Raney, L. M. Carter, P. D. Spudis, H. Hiesinger, and J. H. Pasckert (2014) The Miniature Radio Frequency instrument's (Mini-RF) global observations of Earth's Moon. *Icarus*, *243*, 173-190, 10.1016/j.icarus.2014.07.018.

Campbell, B. A., L. M. Carter, D. B. Campbell, M. Nolan, J. Chandler, R. R. Ghent, B. Ray Hawke, R. F. Anderson, and K. Wells (2010) Earth-based 12.6-cm wavelength radar mapping of the Moon: New views of impact melt distribution and mare physical properties. *Icarus*, *208*, 565-573 10.1016/j.icarus.2010.03.011.

Carter, L. M., C. D. Neish, D. B. J. Bussey, P. D. Spudis, G. W. Patterson, J. T. Cahill, and R. K. Raney (2012) Initial observations of lunar impact melts and ejecta flows with the Mini-RF radar. *J. Geophys. Res.*, *117*, 010.1029/2011JE003911.

Cintala, M.J., K.M. McBride (1995) Block Distributions on the Lunar Surface: A Comparison Between Measurements Obtained from Surface and Orbital Photography. *NASA Technical Memorandum* 104804.

Denevi, B. W., S. D. Koeber, M. S. Robinson, W. B. Garry, B. R. Hawke, T. N. Tran, S. J. Lawrence, L. P. Keszthelyi, O. S. Barnouin, C. M. Ernst, and L. L. Tornabene (2012) Physical constraints on impact melt properties from Lunar Reconnaissance Orbiter Camera images. *Icarus*, *219*, 665-675 10.1016/j.icarus.2012.03.020.

Ghent, R. R., P. O. Hayne, J. L. Bandfield, B. A. Campbell, C. C. Allen, L. M. Carter, and D. A. Paige (2014) Constraints on the recent rate of lunar ejecta breakdown and implications for crater ages. *Geology*, *42*, 1059-1062 10.1130/G35926.1.

Glass, B. P., M. B. Swincki, and P. A. Zwart (1979) Australasian, Ivory Coast and North American

tektite strewnfields - Size, mass and correlation with geomagnetic reversals and other earth events. *Lunar Planet. Sci. Conf.*, *10*, 2535-2545

Hawke, B. R., Head, J.W., 1977. Impact melt on lunar crater rims. In: *Impact and explosion cratering: Planetary and terrestrial implications*, Pergamon Press, New York, pp. 815–841.

Hiesinger, H., C. H. van der Bogert, J. H. Pasckert, L. Funcke, L. Giacomini, L. R. Ostrach, and M. S. Robinson (2012) How old are young lunar craters? *J. Geophys. Res.*, *117*, E00H1010.1029/2011JE003935.

Hood, L. L. and N. A. Artemieva (2008) Antipodal effects of lunar basin-forming impacts: Initial 3D simulations and comparisons with observations. *Icarus*, *193*, 485-502 10.1016/j.icarus.2007.08.023.

Horai, K.-I. and G. Simmons (1972) Thermal property measurements on lunar material returned by Apollo 11 and 12 missions. *Progress in Astronautics and Aeronautics*, *28*, 243-267.

Jögi, P. M. and D. A. Paige (2015) Directed Cratering Ejecta Ballistic Model For Antipodal Impact, Frictionally Heated, Melt Deposits On The Moon. *Lunar Planet. Sci. Conf.*, *46*, 2779

Jögi, P. M. and D. A. Paige (2014) A Ballistic Model for Antipodal Impact Melt Deposits on the Moon. *Lunar Planet. Sci. Conf.*, *45*, 2574

Keller, J., et al. (2015) LRO Mission summary paper, Submitted to *Icarus*, this issue.

Kring, D. A. and D. D. Durda (2002) Trajectories and distribution of material ejected from the Chicxulub impact crater: Implications for postimpact wildfires. *J. Geophys. Res.*, *107*, 506210.1029/2001JE001532.

Moore, H. J., C. A. Hodges, and D. H. Scott (1974), Multiringed basins – Illustrated by Orientale and associated features, *Proc. Lunar Sci. Conf. 5*, 71–100.

Neish, C. D., J. Madden, L. M. Carter, B. R. Hawke, T. Giguere, V. J. Bray, G. R. Osinski, and J. T. S. Cahill (2014) Global distribution of lunar impact melt flows. *Icarus*, *239*, 105–117, 10.1016/j.icarus.2014.05.049.

Neish, C. D., D. T. Blewett, J. K. Harmon, E. I. Coman, J. T. S. Cahill, and C. M. Ernst (2013). A comparison of rayed craters on the Moon and Mercury. *J. Geophys. Res.*, *118*, 2247–2261, 10.1002/jgre.20166.

Neukum, G. and B. Koenig (1976) Dating of individual lunar craters. *Lunar Planet. Sci. Conf.*, *7*, 2867-2881.

Nozette, S., et al. (2010) The Lunar Reconnaissance Orbiter Miniature Radio Frequency (Mini-RF) Technology Demonstration. *Space Sci. Rev.*, *150*, 285-302 10.1007/s11214-009-9607-5.

Paige, D. A., J.-P. Williams, M. T. Sullivan, and B. T. Greenhagen (2011) LRO Diviner Lunar Radiometer global mapping results and gridded data product, *Lunar Planet. Sci. Conf.*, *42*, 2544.

Paige, D. A., et al. (2010) The Lunar Reconnaissance Orbiter Diviner Lunar Radiometer Experiment. *Space Sci. Rev.*, *150*, 125–160 10.1007/s11214-009-9529-2.

Raney, R. K., J. T. S. Cahill, G. W. Patterson, and D. B. J. Bussey (2012) The m-chi decomposition of hybrid dual-polarimetric radar data with application to lunar craters. *J. Geophys. Res.*, *117*, E00H2110.1029/2011JE003986.

Robinson, M. S., P. C. Thomas, J. B. Plescia, B. W. Denevi, K. N. Burns, E. B. Cisneros, M. R. Henriksen, C. H. van der Bogert, H. Hiesinger, P. Mahanti, R.W. Stelling, R. Z. Povilaitis (2015) An Exceptional Grouping of Lunar Highland Smooth Plains: Geography, Morphology, and Possible Origins. *Icarus*, in review.

Robinson, M. S., P. C. Thomas, T. Tran, B. W. Denevi, E. B. Cisneros, J. Plescia, C. H. van der Bogert, and H. Hiesinger (2011) Highland Smooth Plains, an Exceptional Grouping. *Lunar Planet. Sci. Conf.*, *42*, 2511.

Robinson, M. S., et al. (2010) Lunar Reconnaissance Orbiter Camera (LROC) Instrument Overview. *Space Science Rev.*, *150*, 81-124 10.1007/s11214-010-9634-2.

Scholten, F., J. Oberst, K.-D. Matz, T. Roatsch, M. Wählisch, E. J. Speyerer, and M. S. Robinson (2012) GLD100: The near-global lunar 100 m raster DTM from LROC WAC stereo image data. *J. Geophys. Res.*, *117*, E00H1710.1029/2011JE003926.

Schultz, P. H. (1976) *Moon morphology: Interpretations based on Lunar Orbiter photography*. Austin, University of Texas Press, 1976. 641 p.

Stopar, J. D., B. R. Hawke, M. S. Robinson, B. W. Denevi, T. A. Giguere, and S. D. Koeber (2014) Occurrence and mechanisms of impact melt emplacement at small lunar craters. *Icarus*, *243*, 337-357 10.1016/j.icarus.2014.08.011.

Vasavada, A.R., D.A. Paige, and S.E. Wood (1999) Near-Surface Temperatures on Mercury and the Moon and the Stability of Polar Ice Deposits. *Icarus*, *141*, 179-193 10.1006/icar.1999.6175.

Wells, K. S., D. B. Campbell, B. A. Campbell, and L. M. Carter (2010) Detection of small lunar secondary craters in circular polarization ratio radar images. *J. Geophys. Res.*, *115*, E0600810.1029/2009JE003491.

Williams, J.-P., E. Sefton-Nash, and D. A. Paige (2015) The temperatures of Giordano Bruno crater observed by the Diviner Lunar Radiometer Experiment: applicaiton of an effective field of view model for a point-based data set. *Icarus*, submitted (this issue).

Xiao, Z., Z. Zeng, N. Ding, and J. Molaro (2013) Mass wasting features on the Moon - how active is the lunar surface? *Earth Planet. Sci. Lett.*, *376*, 1-11 10.1016/j.epsl.2013.06.015.

Zanetti, M. A. Stadermann, B. Jolliff, C. H. van der Bogert, H. Hiesinger, J. B. Plecia (2015) Auto-secondary cratering vs. target property effect on ejecta blankets of Copernican craters: What are the implications for age dating using small-diameter crater statistics? *Lunar Planet. Sci. Conf.*, *46*, 1209.

Figure Captions

Figure 1. LRO NAC image M1100101542L, centered near 167.6°E, 43.1°N. The numerous flat areas in local depressions are interpreted by *Robinson et al.* (2015) as melt ponds that are pervasive throughout the region.

Figure 2. Diviner rock abundance maps (color) with the LRO WAC DEM (shading). The top image, centered near 168°E, 43°N, shows rock distributions, which are typically associated with relatively fresh craters. The anomalously rocky Tycho crater antipode region is located near the center of the top image and is shown in detail in the bottom image. The antipode of Tycho crater is denoted by the white "X", and the northern and southern regions of interest are outlined in the bottom image. In the bottom image, the white square indicates the location of the image shown in Figure 6 and the white rectangle in the bottom image indicates the location of the radar data shown in Figure 13.

Figure 3. Diviner Tycho crater antipode rock abundance distributions for the two regions of interest shown in Figure 2. The direction on the polar plots represents the azimuth of the local slope (only slopes >15° are included here) and the radial distance represents the rock abundance. Colors represent the fraction of slopes with a given rock abundance for each slope azimuth. For example, the cyan-colored bin denoted by the arrow for the northern region plot shows that ~1% of slopes (>15°) facing 350–360° have rock abundances of 8–9%. The plots show a strong asymmetry in the rock abundances based on the surface slope azimuth orientations.

Figure 4. Polar plots showing the rock abundance of modeled surfaces that would be protected from incoming material of a particular azimuth/elevation orientation. The two plots are for the northern and southern regions of interest shown in Figure 2. The direction on the polar plots represents the azimuth and the radial distance represents the elevation above the horizon from which the modeled incoming material is traveling. The colors represent the fraction of surfaces that would be protected from incoming material that have low rock abundances (<1% areal coverage). For example, the arrow

in the bottom plot points to a bin that represents a model of incoming material from a direction of 315–320° and 18–20° above the horizon. The red color indicates that almost none of the surfaces that would be protected from material have a high rock abundance. High values on the plots (orange and red) are consistent with the modeled direction of incoming material. The numbers (1–4) on the bottom plot represent examples described in Figure 5. Blank areas on the plots indicate a low total area of surfaces that would be protected in the model (<1000 pixels).

Figure 5. Modeled protected surfaces from incoming material for four azimuth/elevation orientations for the southern region of interest (denoted in Figure 4). Colors represent rock abundances in the Tycho crater antipode region, and is similar to data shown in Figure 2. Bright areas highlight surfaces that would be protected from incoming material for each particular modeled azimuth/elevation orientation. Examples 1 and 2 highlight many surfaces with elevated rock abundances, which is inconsistent with the modeled direction of incoming material. By contrast, most highlighted surfaces in Examples 3 and 4 have low rock abundances, consistent with being protected from an influx of material from the modeled direction. Although, Example 4 highlights rock-free surfaces almost exclusively, there are also many rock-free surfaces in the immediate area that are not highlighted, indicating that incoming material may have come from a lower elevation, such as that similar to Example 3. These results include surfaces that would be protected based on the model that includes ray-tracing.

Figure 6. (top) Surface rock abundance (color) with mosaic of LRO NAC images M111543585L/R and M1100101542L (shading), centered near 43.9°N, 167.9°E (indicated by the white box in Figure 2). The white box shows the area covered by the top image in Figure 7. (bottom) Rock abundance distributions for the area within the oval shown in the top image. The direction on the polar plots represents the azimuth of the local slope (slopes >15° are included) and the radial distance represents the rock abundance, similar to Figure 3. Colors represent the fraction of slopes with a given rock

abundance for each slope azimuth. The high rock abundances on north and west facing slopes are consistent with rocky slope azimuths in the region (shown in Figure 3).

Figure 7. LRO NAC image M111543585L, centered near 43.9°N, 167.9°E (indicated by the white box in Figure 6). The top image shows a portion of the north-facing wall and floor of the crater (denoted by the white circle in Figure 6). Image a) shows a transition from north-facing rocky surfaces to east-facing rock-free surfaces. Image b) shows melt ponds with rubble piles that formed at the intersection between flows. Image c) shows rocky and highly fractured surfaces typical of north- and west-facing slopes in the region. Image c) and the right side of image a) show rocky surfaces that are similar to those that are prevalent throughout the region and identified in the Diviner rock abundance data.

Figure 8. Diviner rock abundance maps (color) with the LRO WAC DEM (shading). The top image, centered near 310°E, 43°S, shows anomalously high rock abundances in the nearside region. The broad region near the center of the image includes highlands terrains that have anomalously high rock abundances. White outlines indicate the three regions of interest described in the text, red/white points show the locations of granular flows, and the yellow box indicates the location of the detailed image (bottom). The detailed image shows the prevalence of rocky surfaces on north and west-facing slopes. White circles show the locations of granular flows and the white arrow shows the location of the radar data showin in Figures 13 and 14..

Figure 9. (top) Diviner nearside rock abundance distributions for the regions of interest shown in Figure 8. The direction on the polar plots represents the azimuth of the local slope (slopes >15° are included) and the radial distance represents the rock abundance. Colors represent the fraction of slopes with a given rock abundance for each slope azimuth. The plot shows asymmetry in the rock abundances based on the surface slope azimuth orientations, most visibly at the larger rock abundance ranges. West- and north-facing slopes have higher rock abundances in the region than south- and east-

facing slopes. (bottom) Polar plots showing the rock abundance of modeled surfaces that would be protected from incoming material of a particular azimuth/elevation orientation. The direction on the polar plots represents the azimuth and the radial distance represents the elevation above the horizon from which the modeled incoming material is traveling. The colors represent the fraction of surfaces that would be protected from incoming material that have low rock abundances (<1% areal coverage). High values on the plots (orange and red) are consistent with the modeled direction of incoming material. Blank areas on the plots indicate a low total area of surfaces that would be protected in the model (<1000 pixels).

Figure 10. LRO NAC image M124924825R, centered near 305.86°E, 36.61°S. Rocks are distributed across a northwest-facing slope. These features are common throughout the nearside anomalously rocky region.

Figure 11. Mosaic of LRO NAC images M104856782L/R, centered near 308.05°E, 39.72°S. Rocks and granular flows are distributed along north and northwest facing slopes of the crater. The white box denotes the area of the image shown in Figure 12.

Figure 12. LRO NAC image M104856782L, centered near 308.00°E, 39.76°S. Granular flows are present throughout the area along with rubble piles. The white box in the top image denotes the area shown in the bottom image.

Figure 13. Mini-RF S1 total power images, centered near 167.8°E, 43.0°N (left; lsz_04544_1cd_xku_50n168) and 307.6°E, 40.5°S (right; lsz_03371_1cd_xku_42s307). The left image shows the numerous melt ponds (white oval) and flow features (Arrow 1) present throughout the Tycho crater antipode region. The right image shows radar bright surfaces in the nearside region that are associated with rocky surfaces (Arrow 2) and granular flows on crater walls (Arrow 3). The left image is denoted by the white rectangle in Figure 2 and the location of the right image is shown by the arrow in Figure 8.

Figure 14. Mini-RF M-chi decomposition images (*Raney et al.*, 2012; *Cahill et al.*, 2014), centered near 307.6°E, 40.5°S (lsz_03371_1cd_xku_42s307). The composite image shows the even bounce, volume scattering, and odd bounce images projected as red, green, and blue respectively. The enhanced return from all three parameters indicates that rocky materials are typically present in the near subsurface only where they are present at the surface as well. The images cover the same area shown in the right image of Figure 13 and is at the location shown by the white arrow in Figure 8.

Tables

Table 1: Preferential orientations of rocky and rock-free surfaces near the Tycho crater antipode and nearside regions of interest.

Surfaces with elevated rock concentrations:			
Region	Surface slope azimuth	Surface slope angle	Rocky surfaces (>1% rocks)
Antipode North	180–350°	>15°	60%
Antipode South	240–60°	>15°	69
Nearside	240–330°	>15°	43
Nearside	330°–240°	>15°	18
Surfaces protected from falling material:			
Region	Incoming azimuth	Incoming elevation	Rock-free surfaces (<1% rocks)
Antipode North	75–115°	0–20°	>70%
Antipode South	115–165°	0–20°	>70
Nearside	55–150°	0–20°	>80

Figure 01

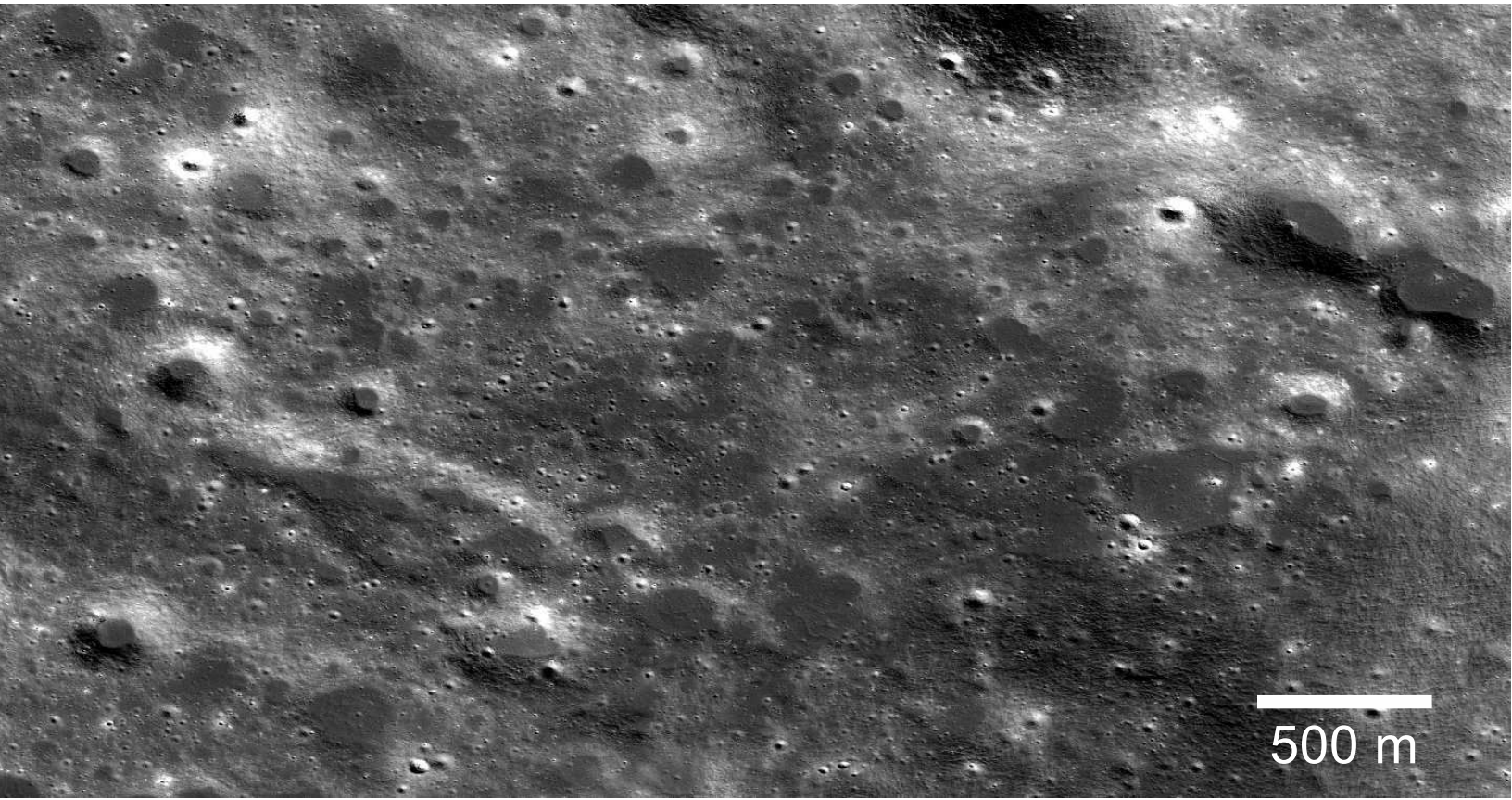

Figure 02

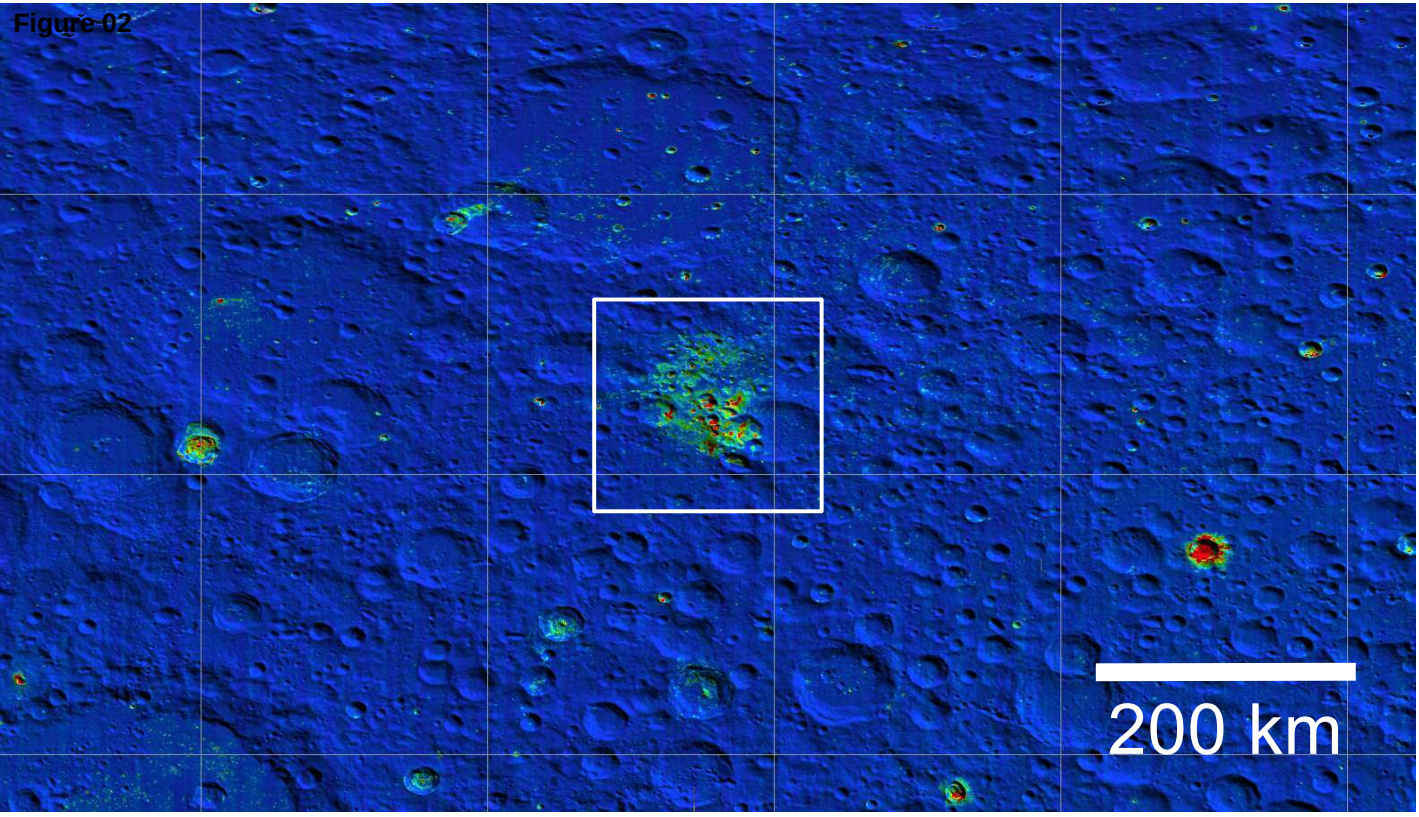

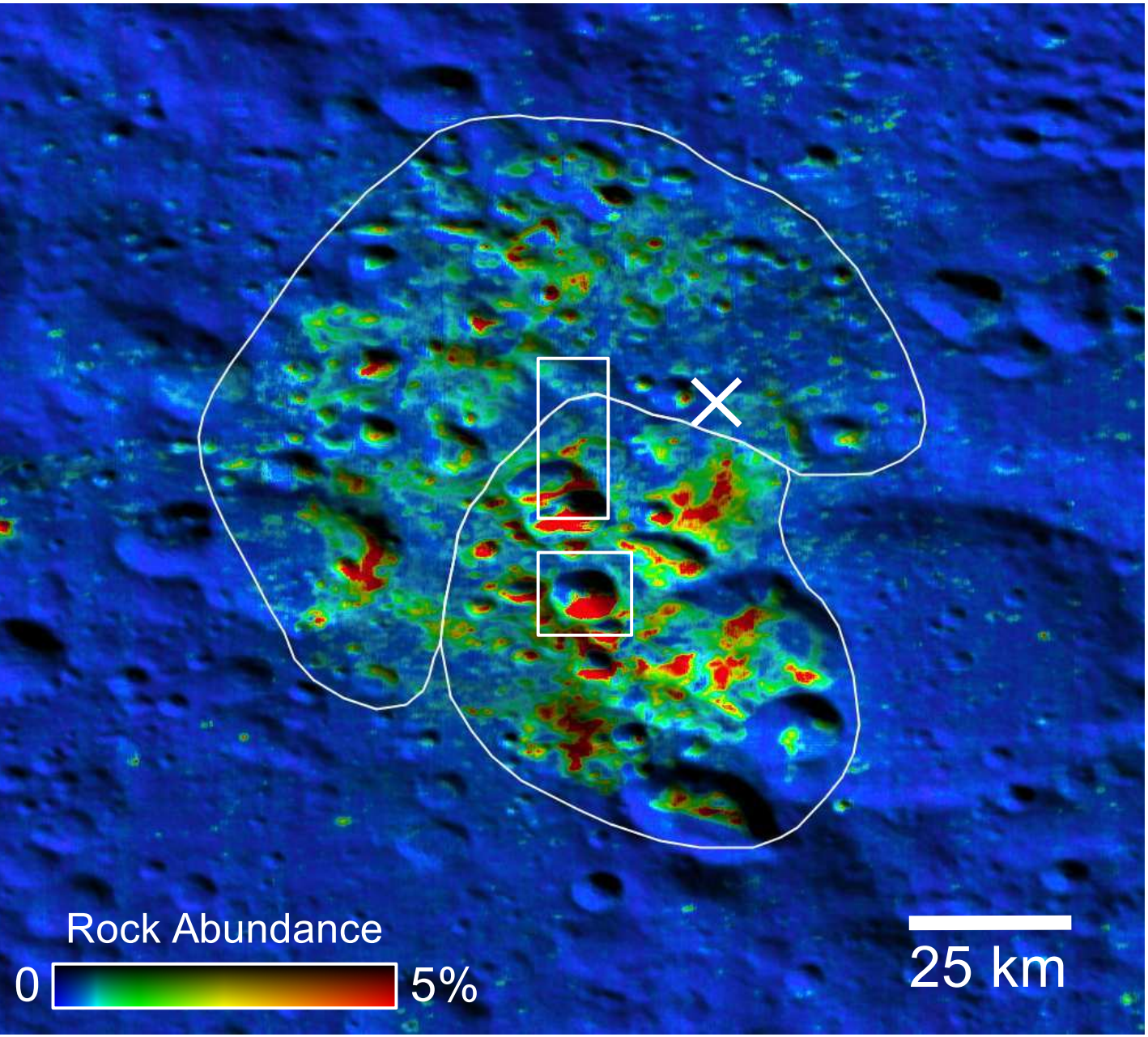

Northern Region

Figure 03

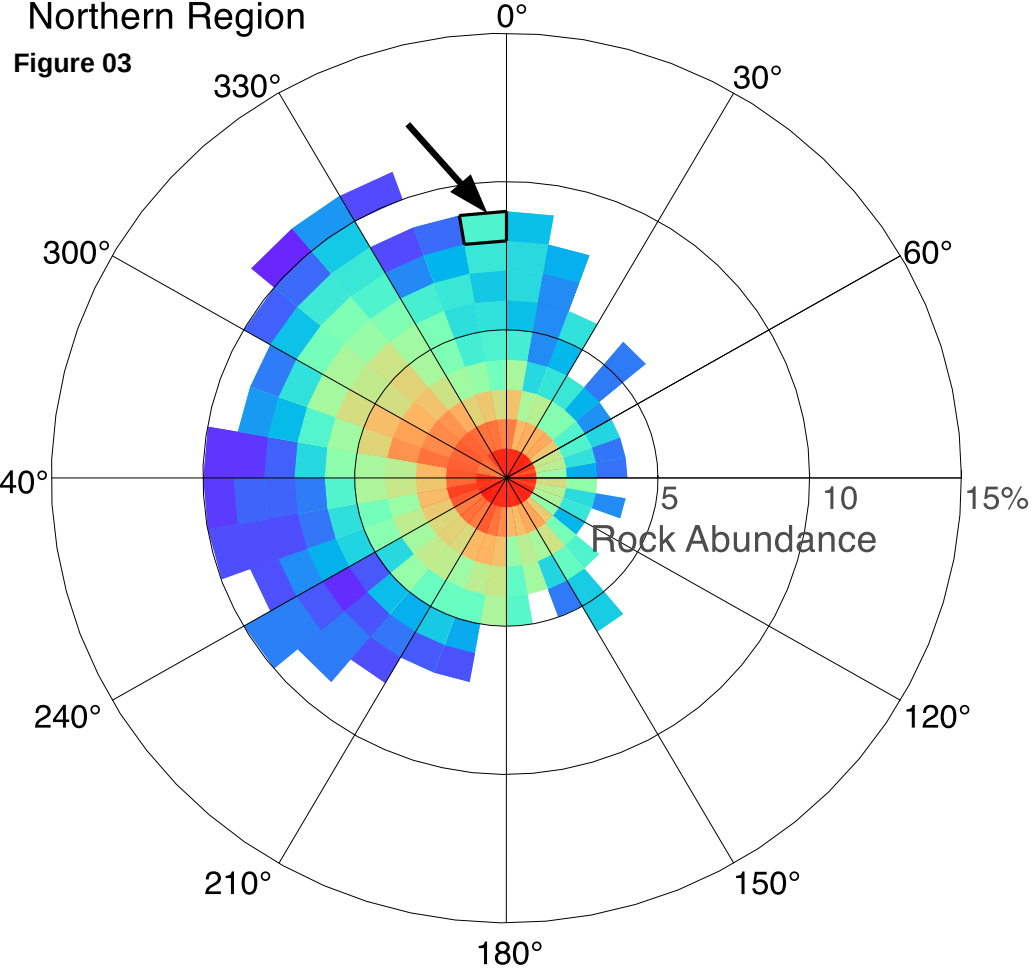

Southern Region

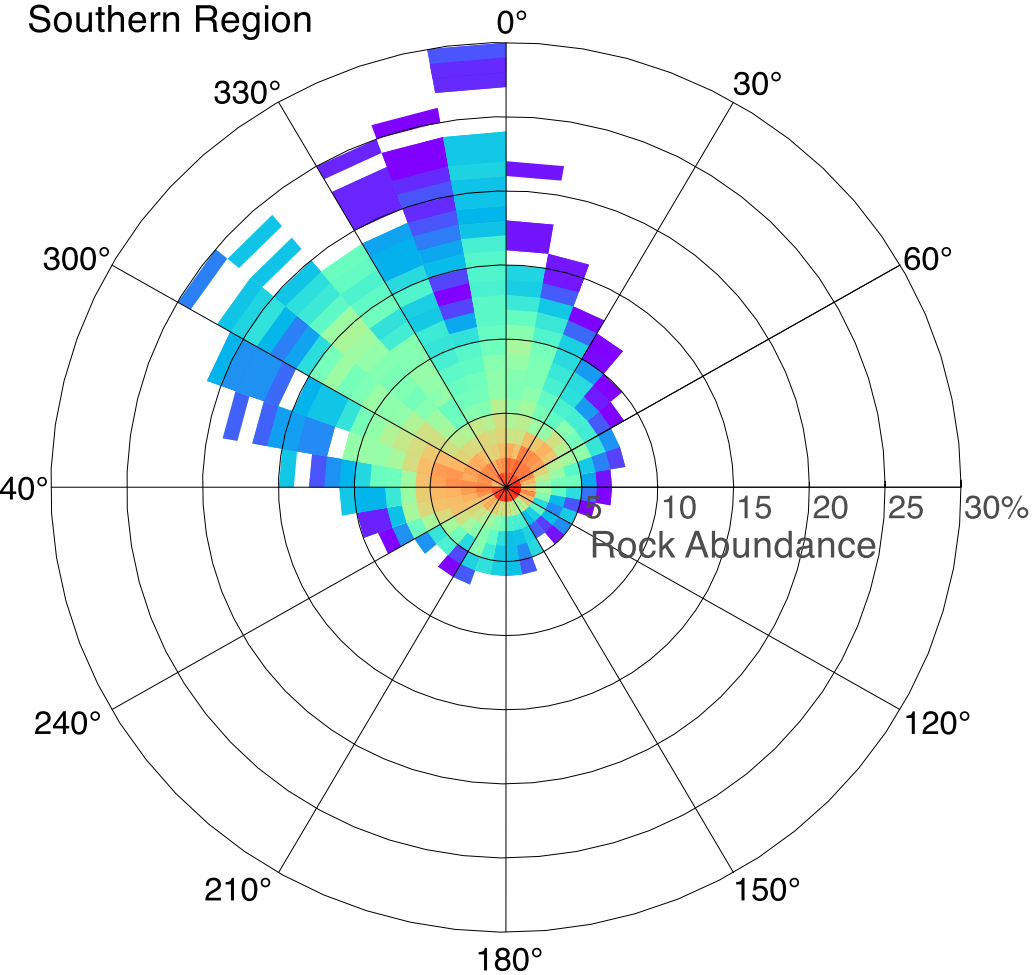

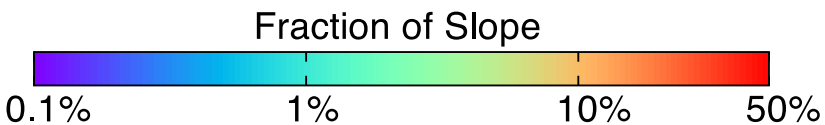

Northern Region

Figure 04

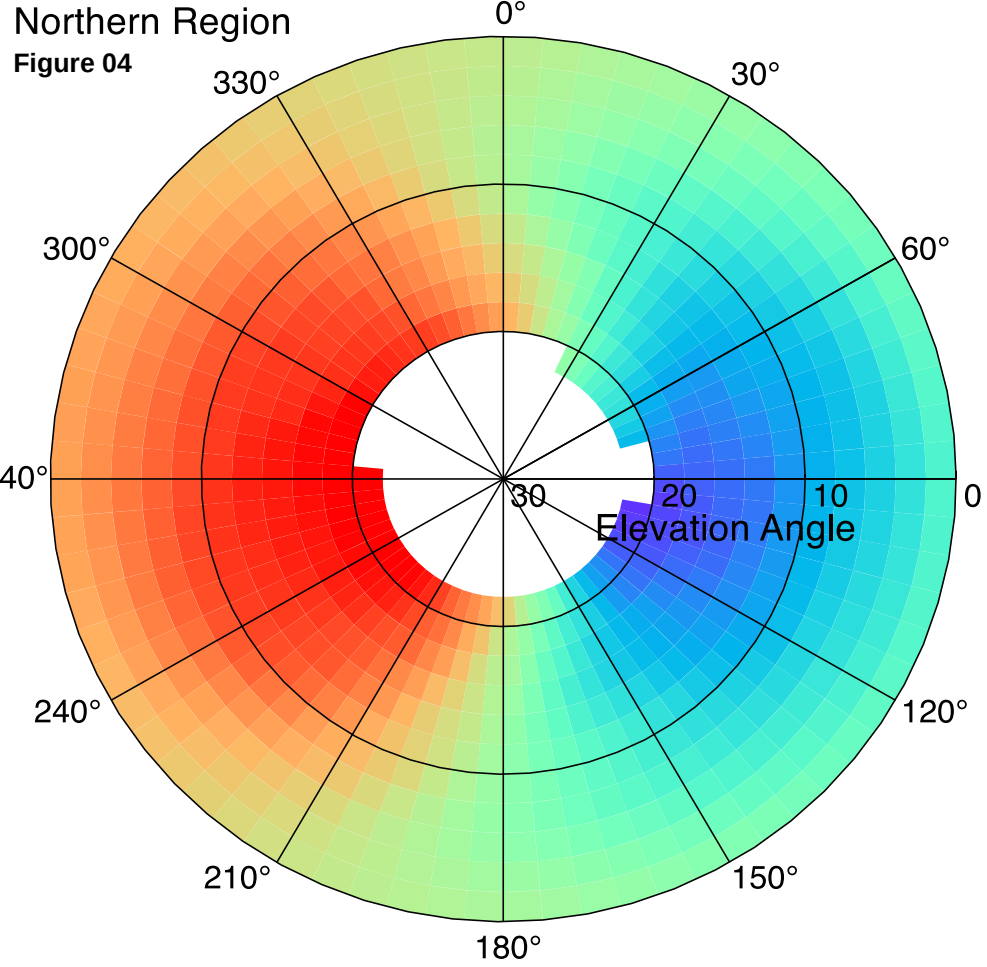

Southern Region

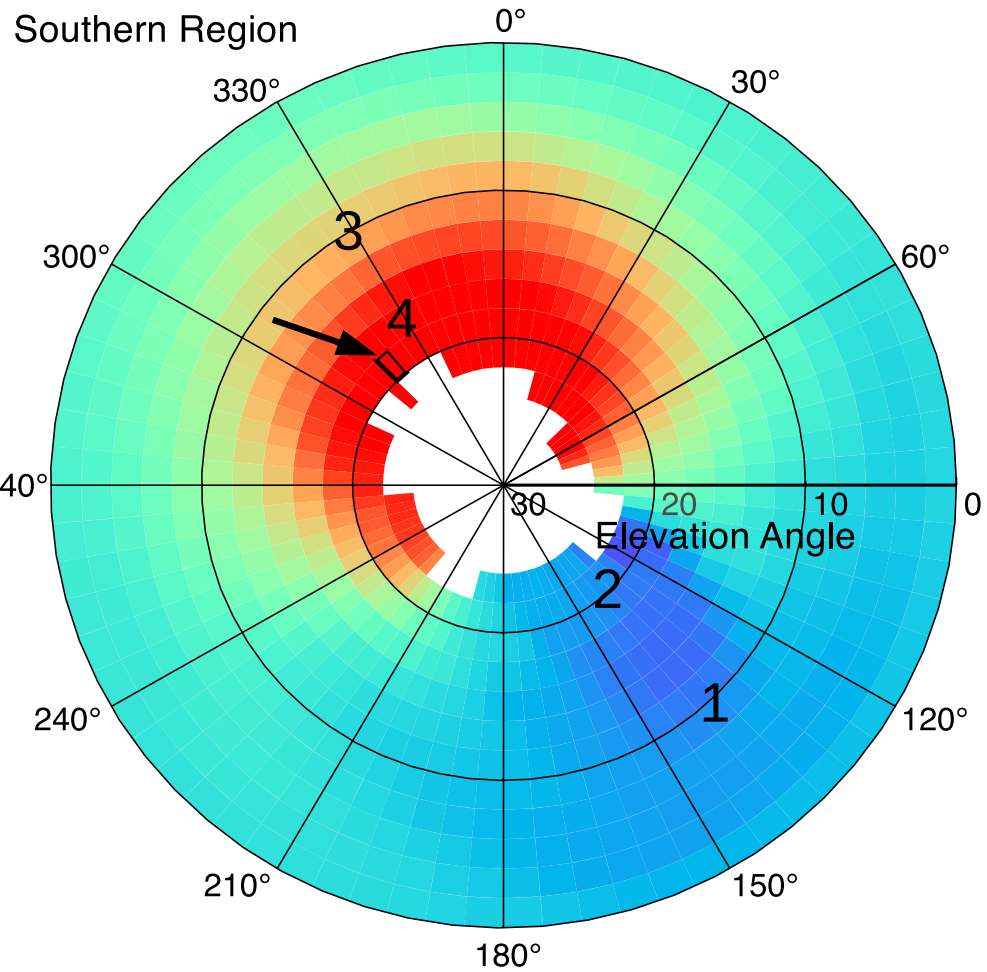

Fraction of Rock-free Protected Surfaces

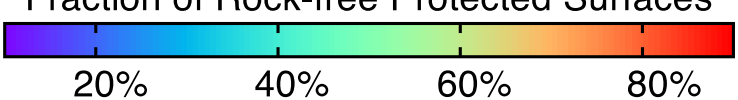

Figure 05

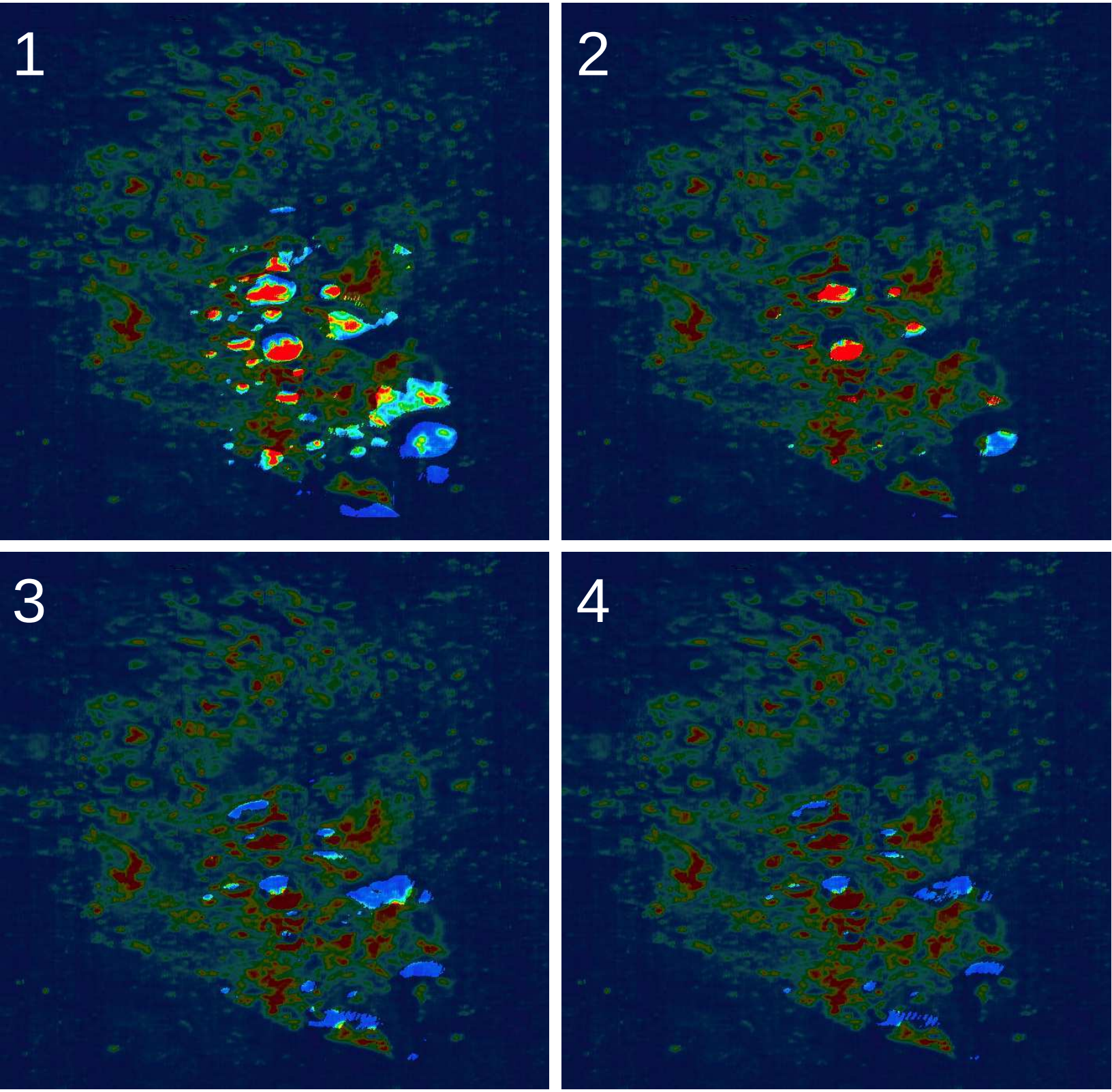

Figure 06

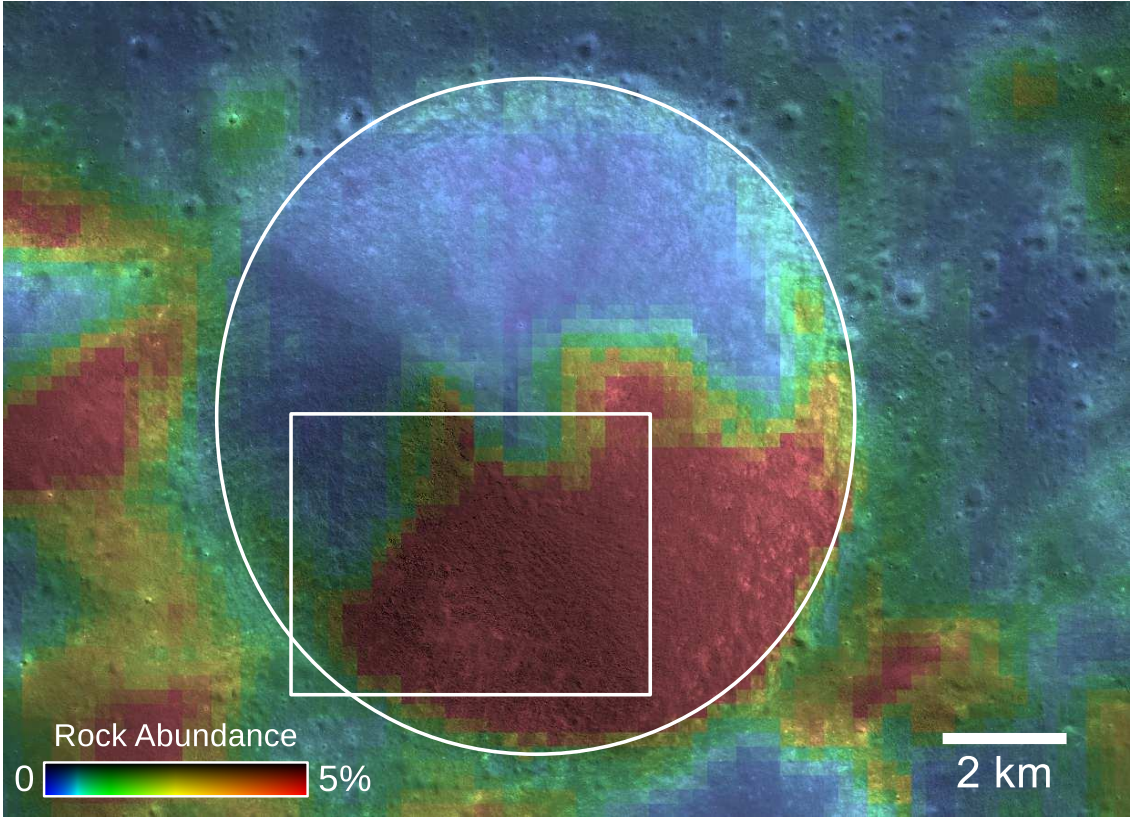
Rock Abundance
0
5%
2 km

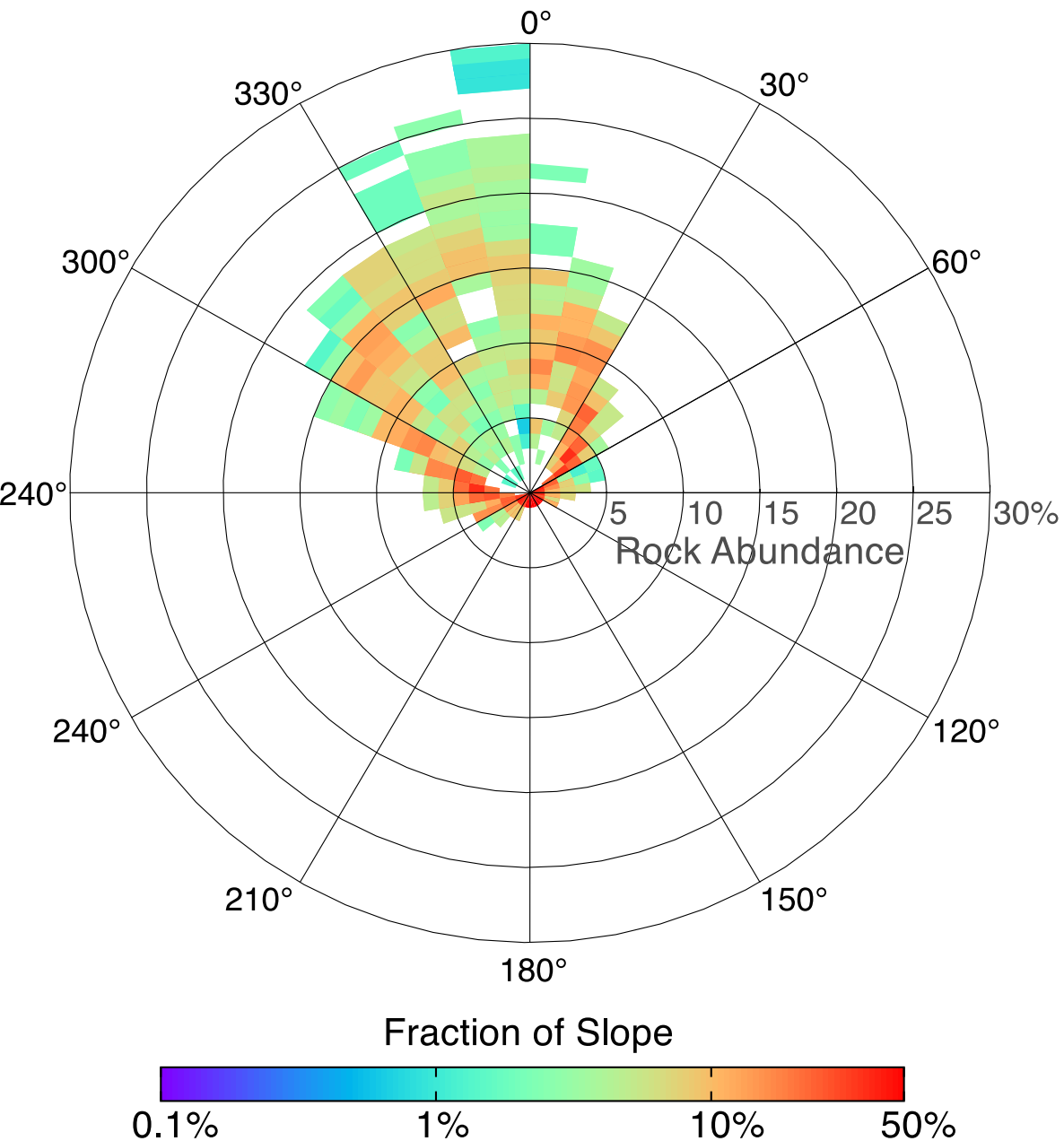
0°
30°
60°
120°
150°
180°
210°
240°
300°
330°
5
10
15
20
25
30%
Rock Abundance
Fraction of Slope
0.1%
1%
10%
50%

Figure 07

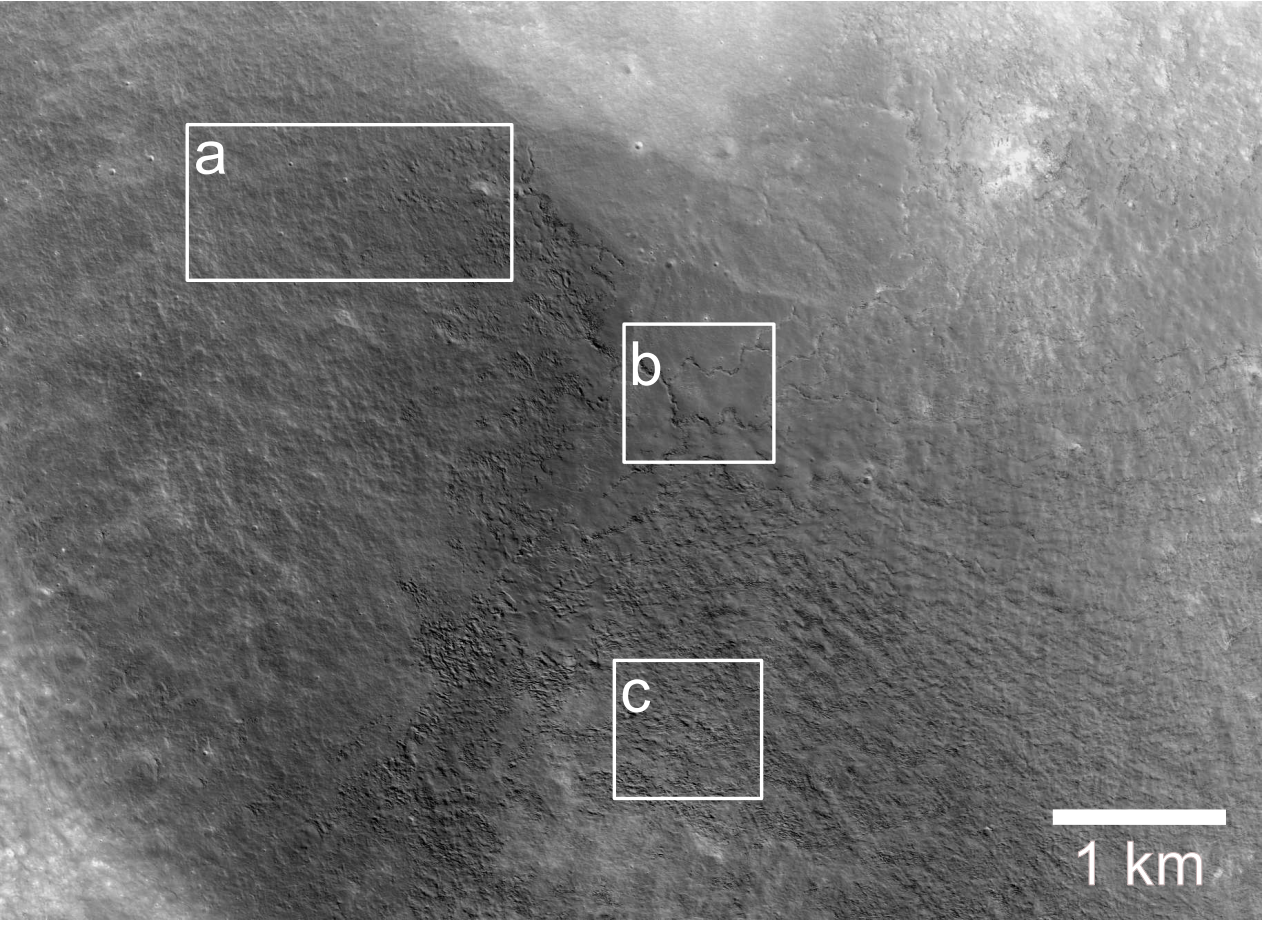

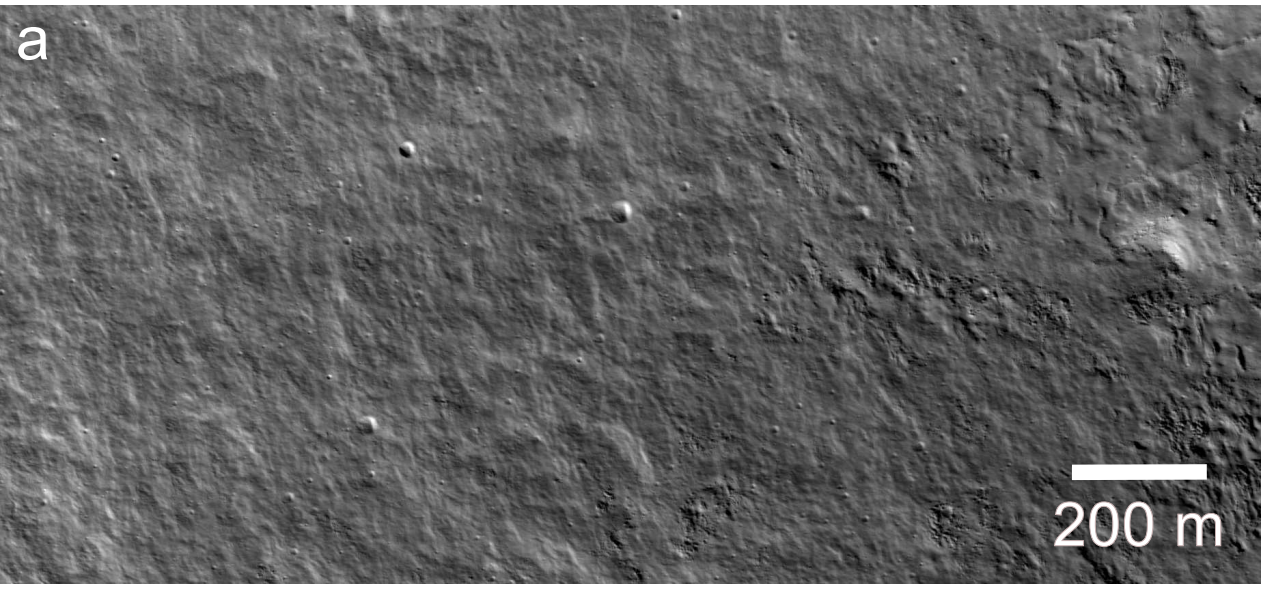

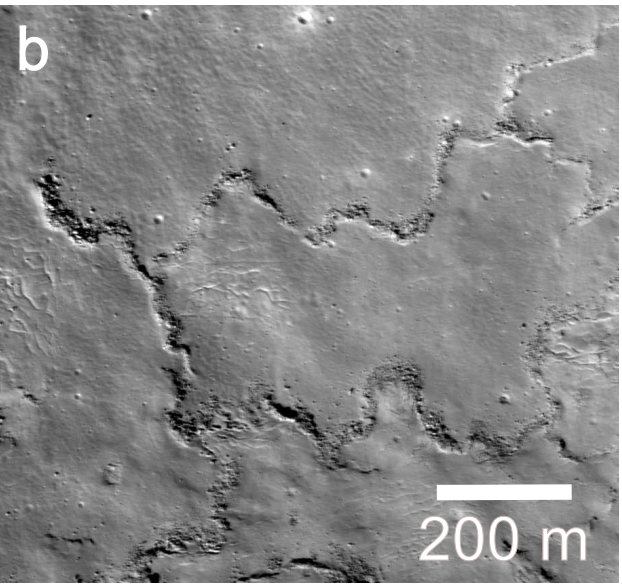

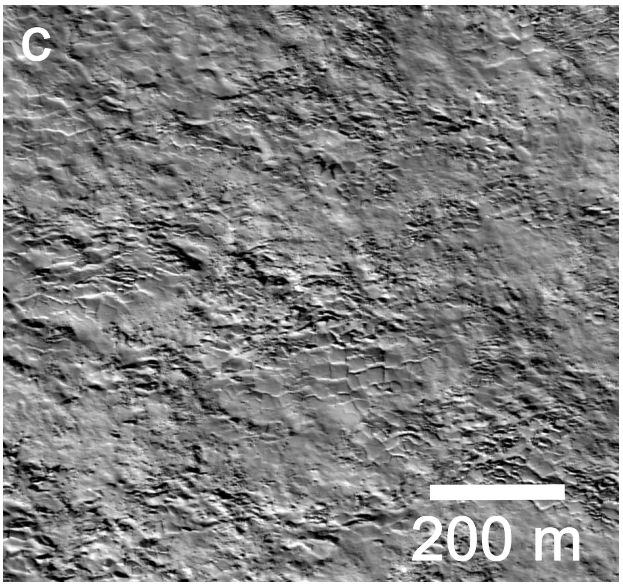

Figure 08

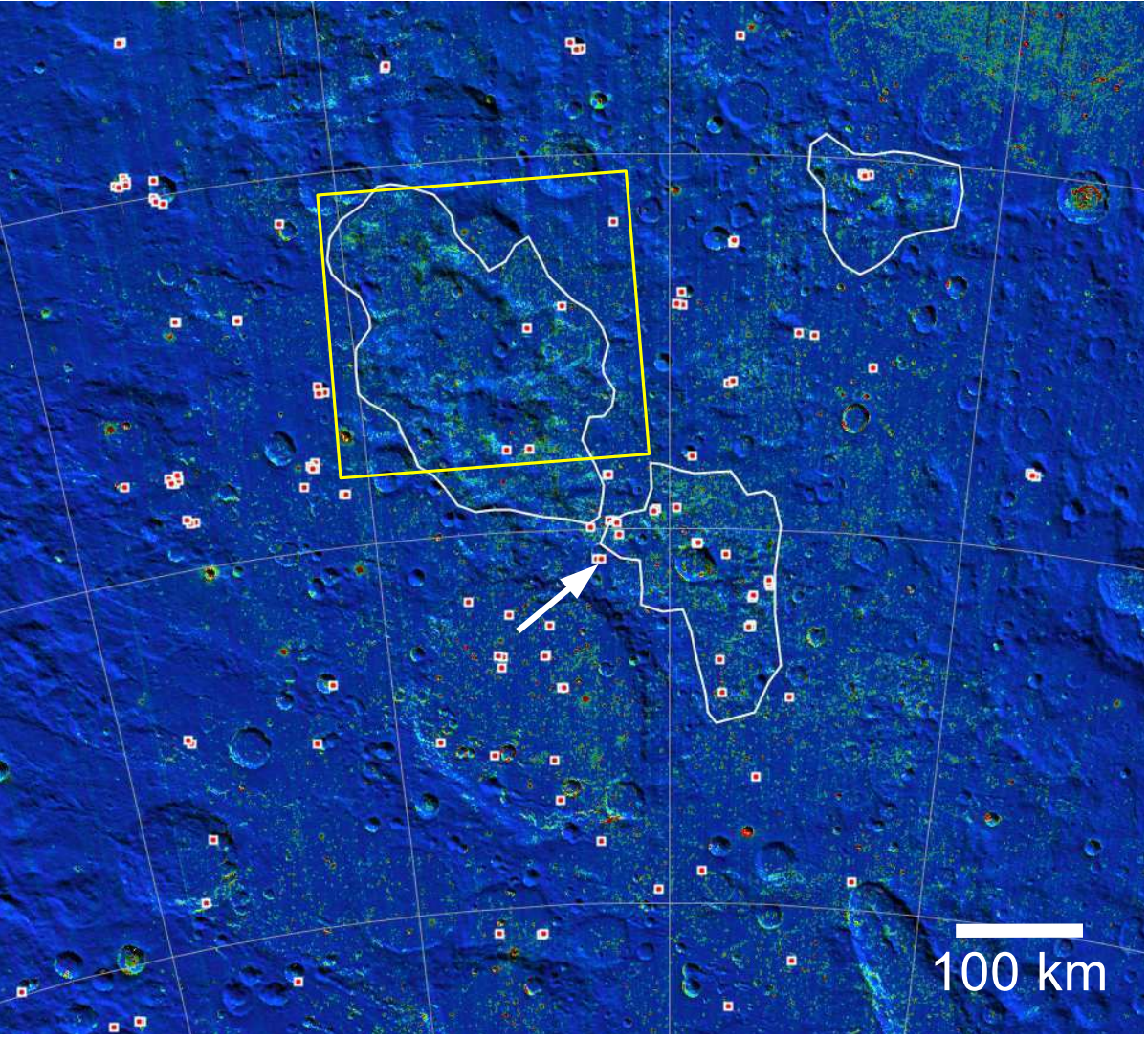

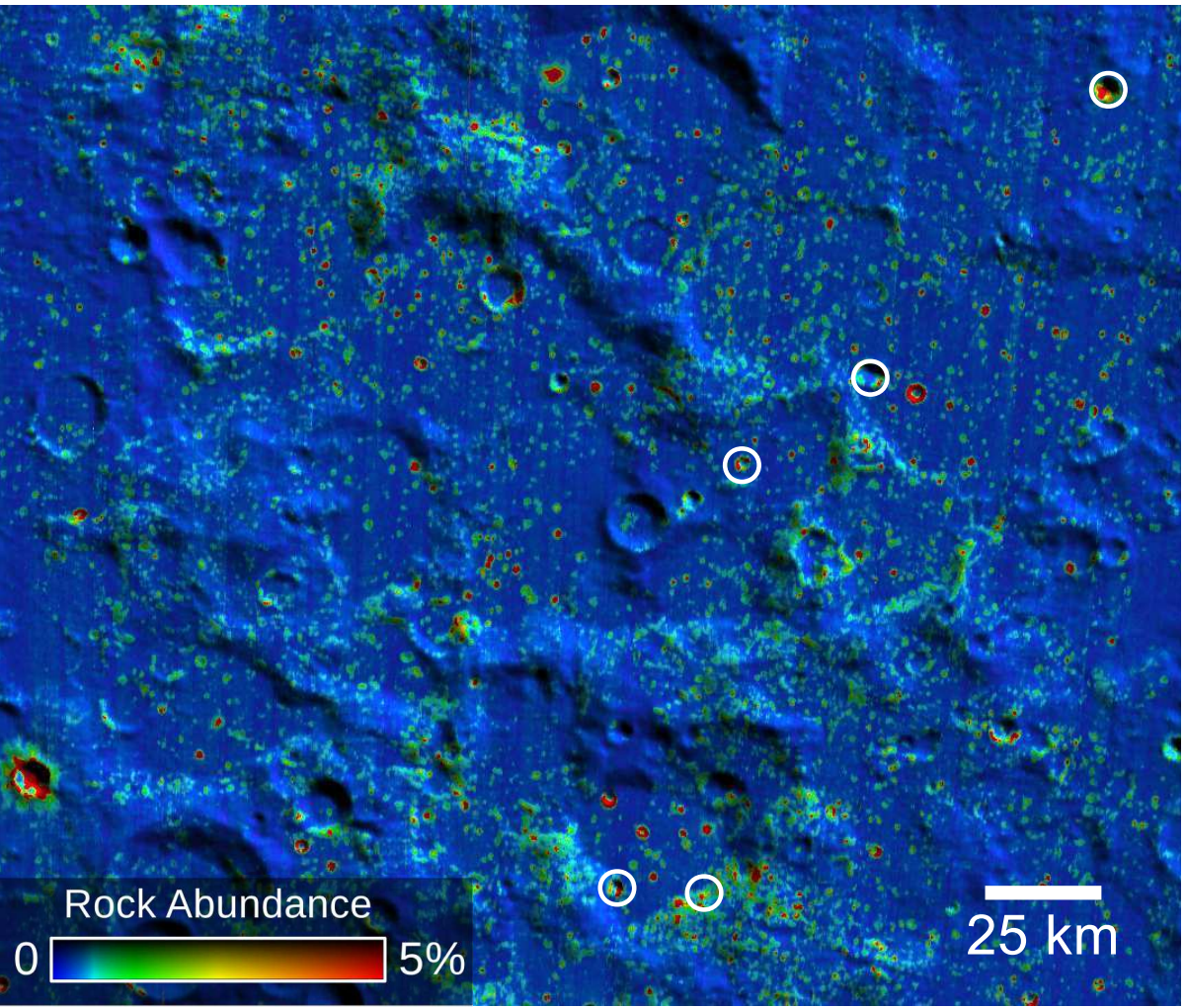

Figure 09

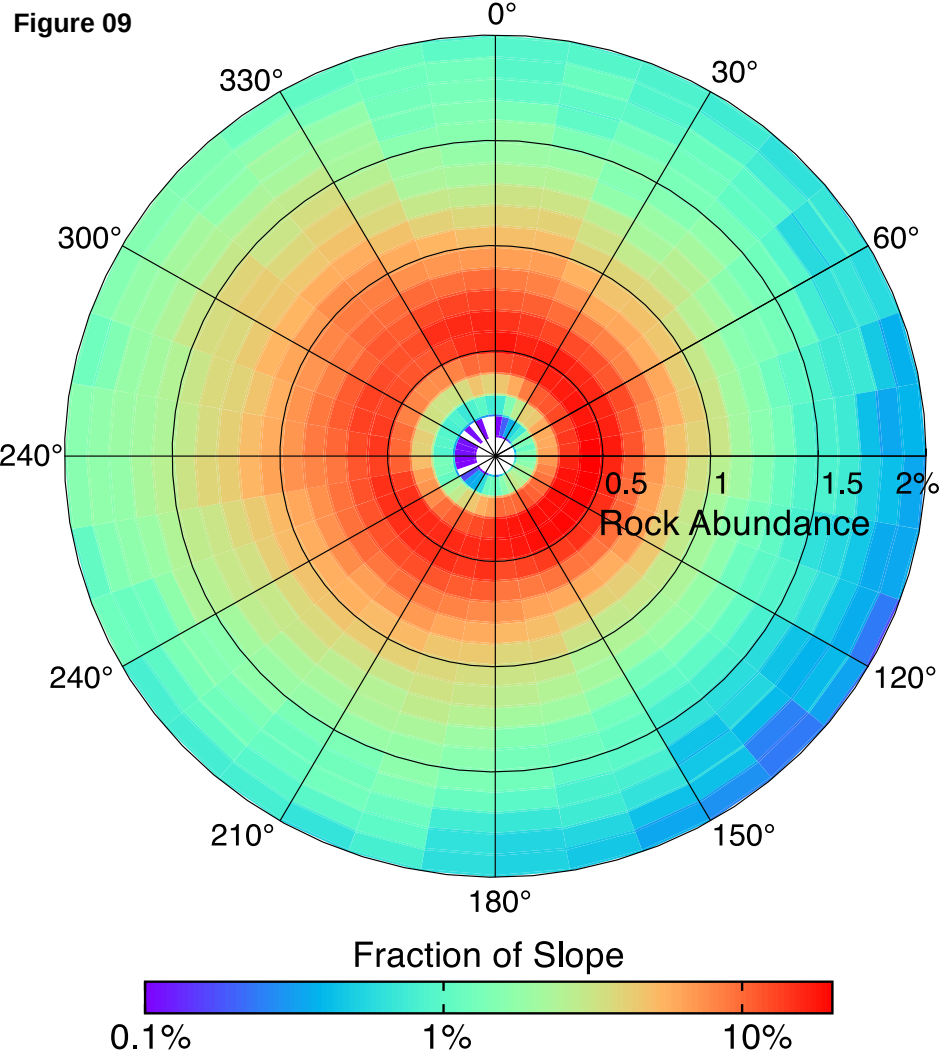
0°
30°
60°
120°
150°
180°
210°
240°
300°
330°
0.5
1
1.5
2%
Rock Abundance

Fraction of Slope
0.1%
1%
10%

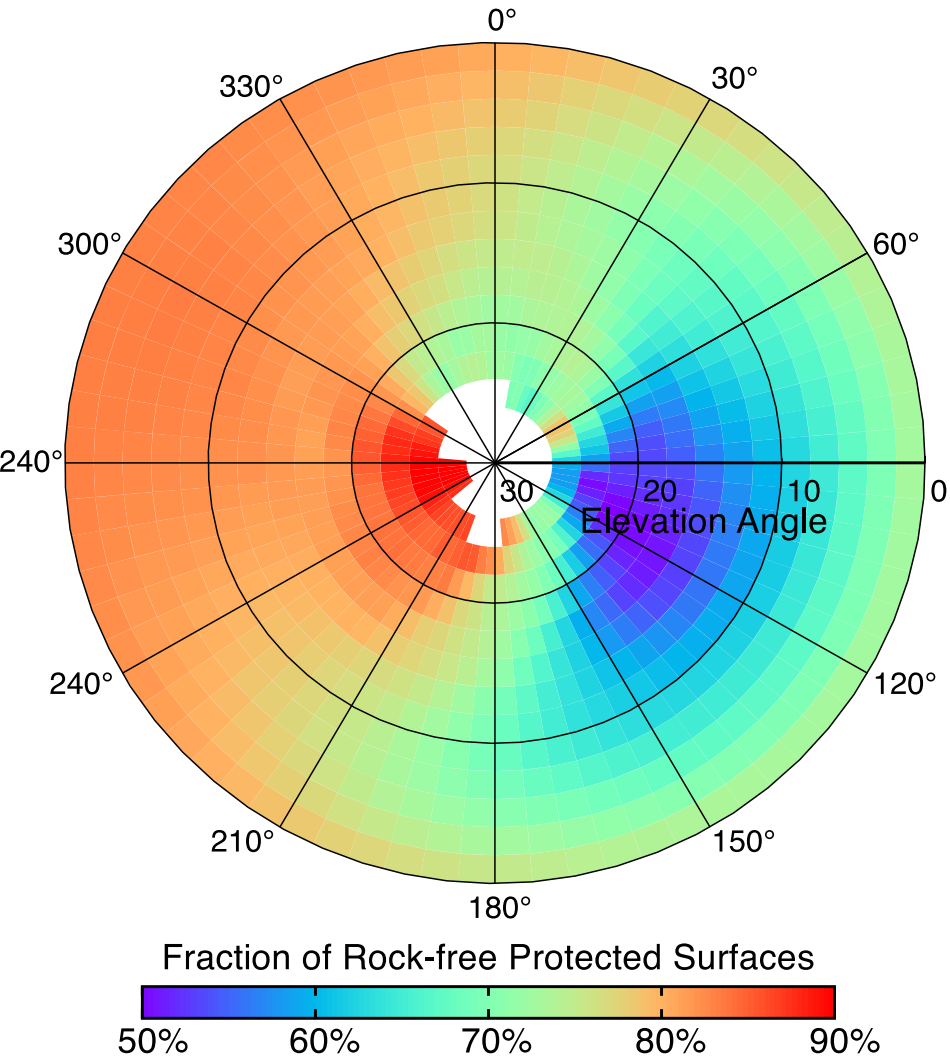
0°
30°
60°
120°
150°
180°
210°
240°
300°
330°
30
20
10
0
Elevation Angle

Fraction of Rock-free Protected Surfaces
50%
60%
70%
80%
90%

Figure 10

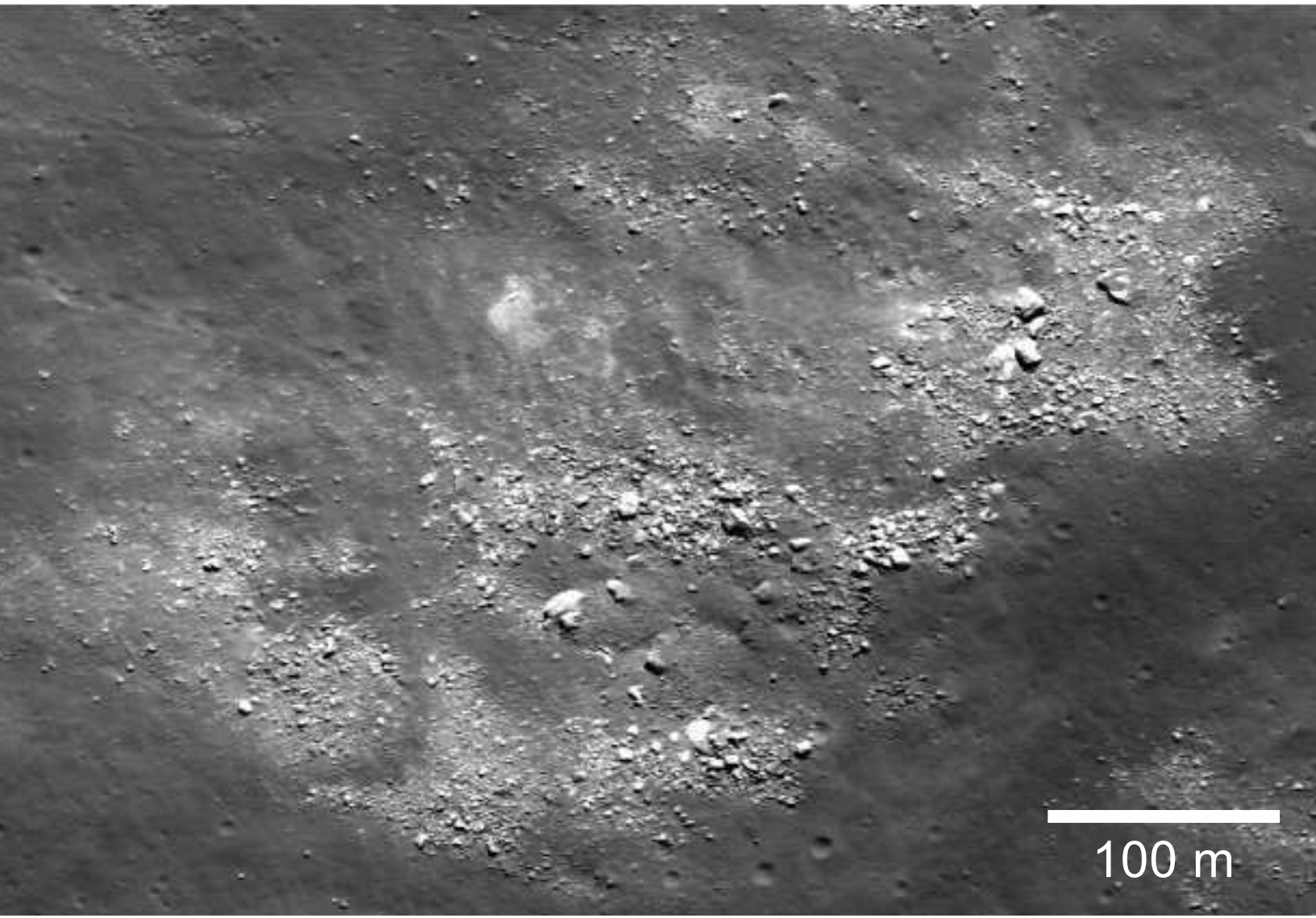

Figure 11

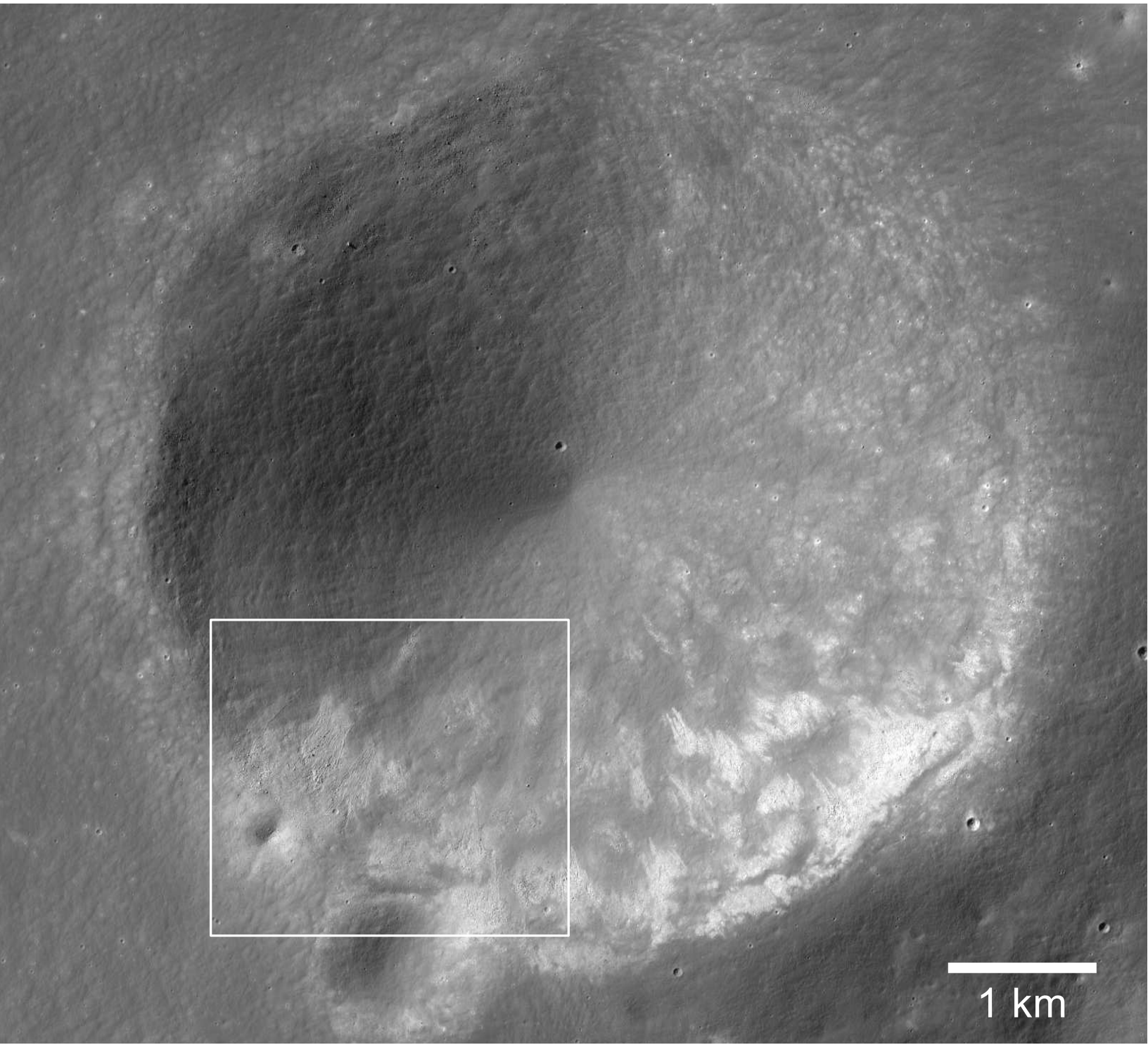

Figure 12

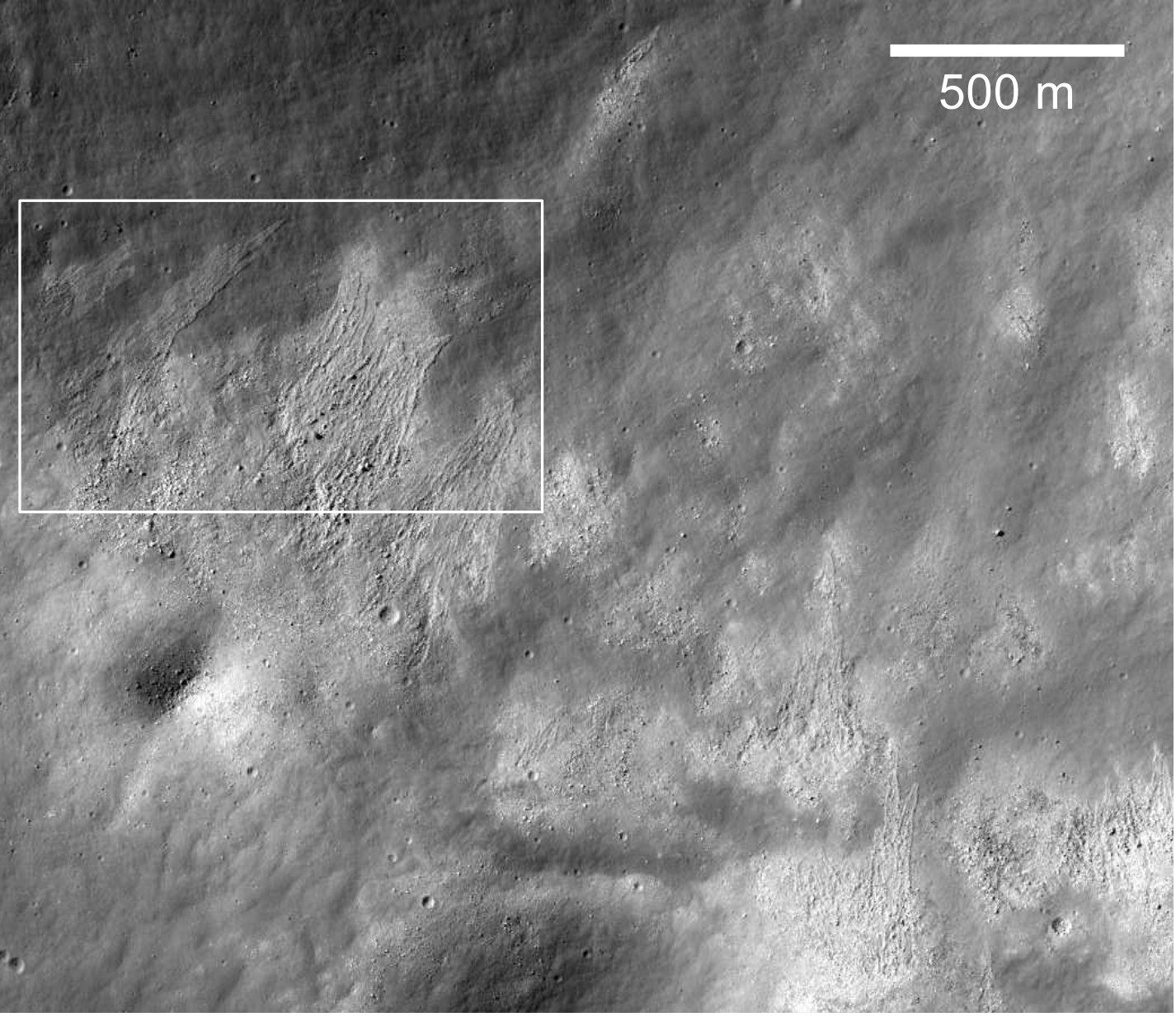

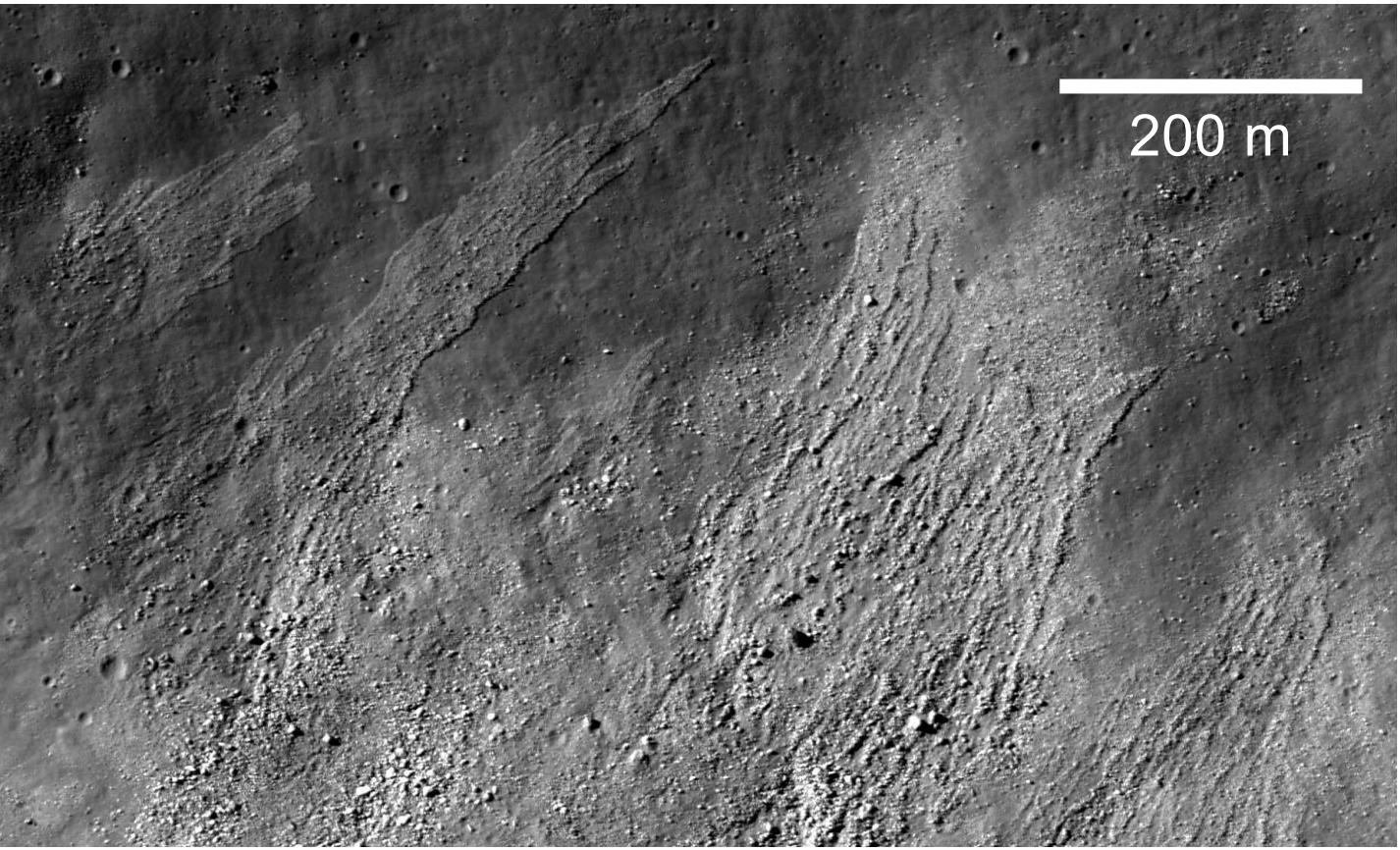

Figure 13

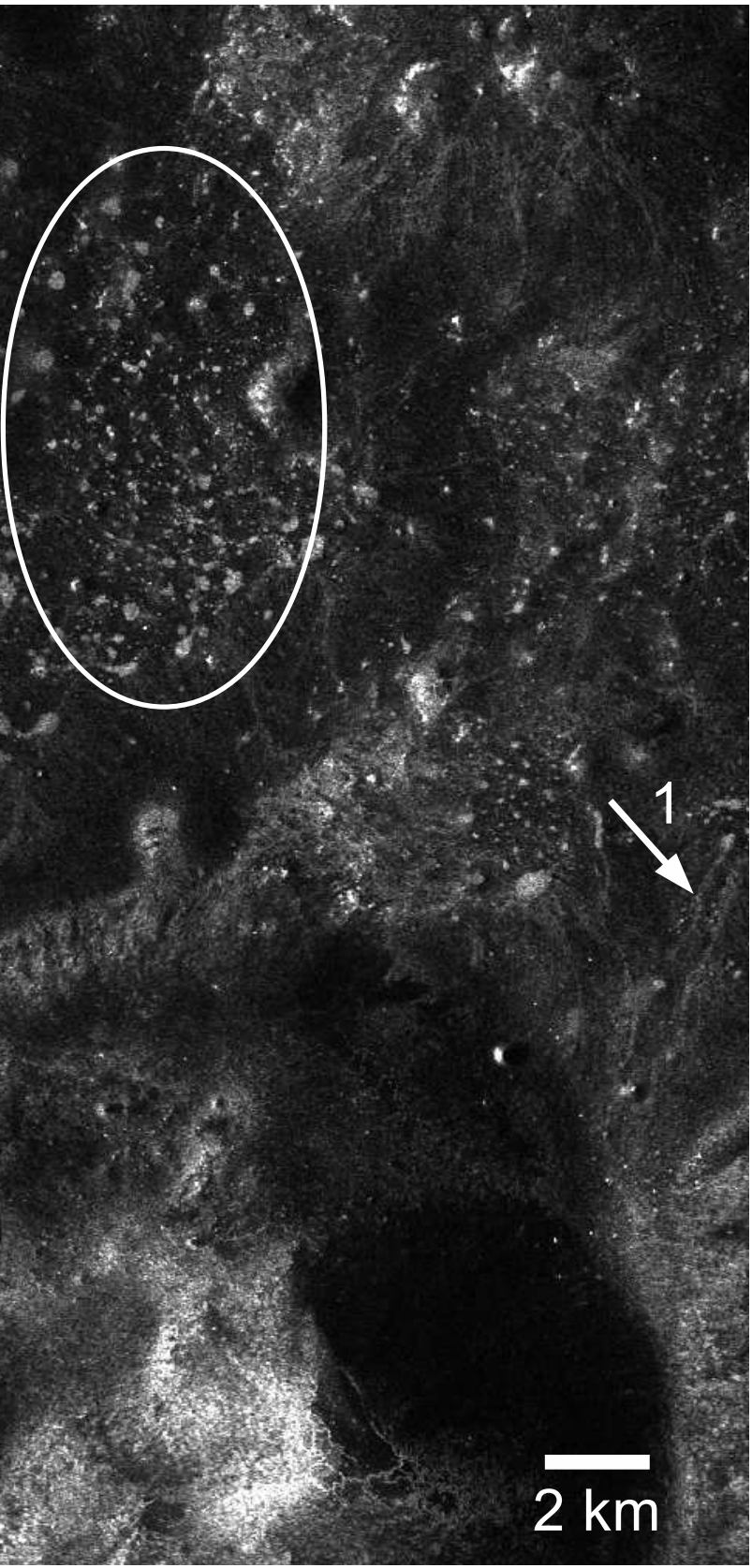

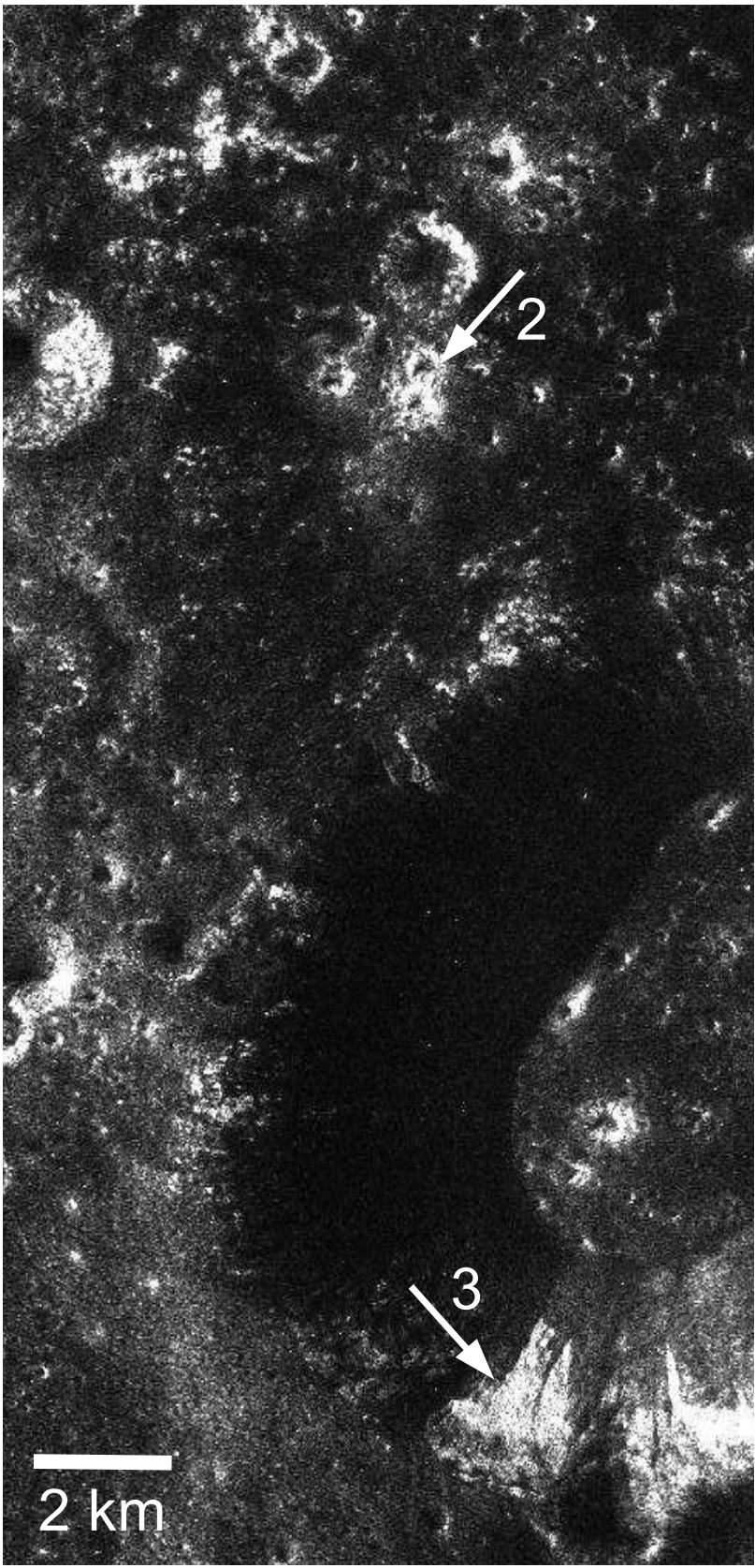

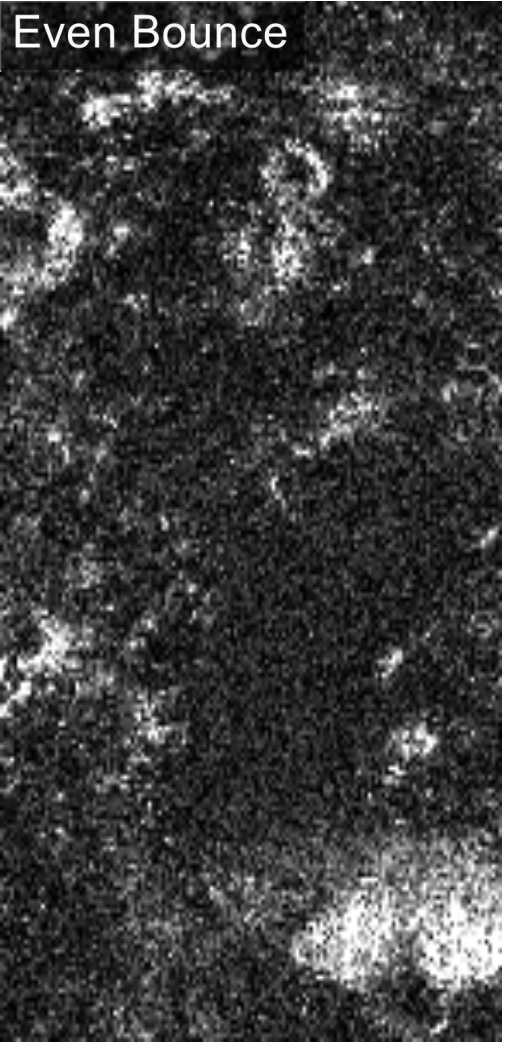

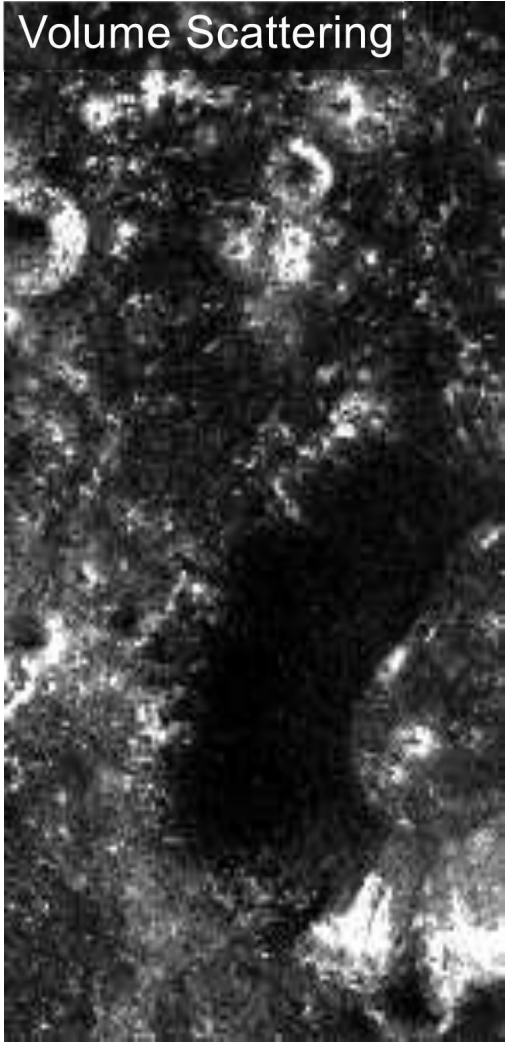

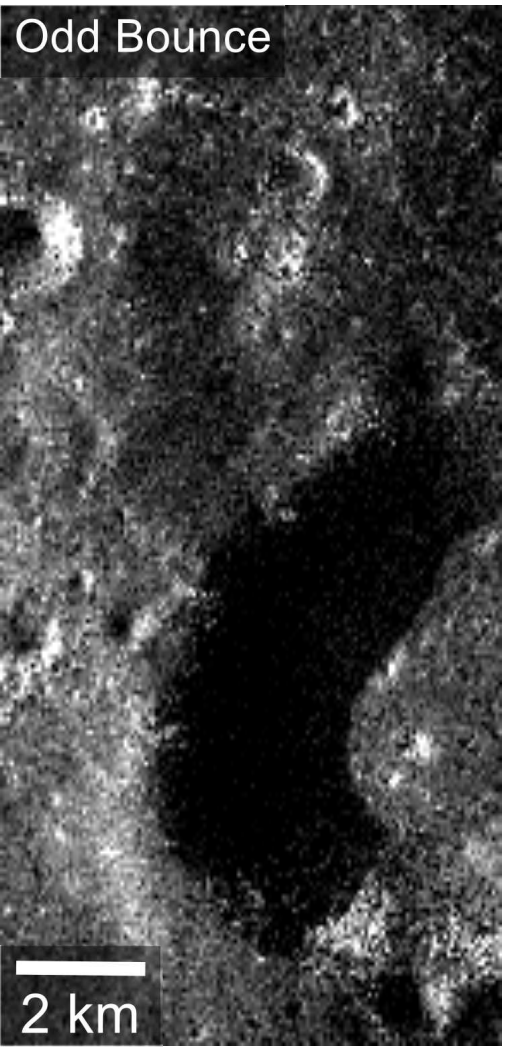

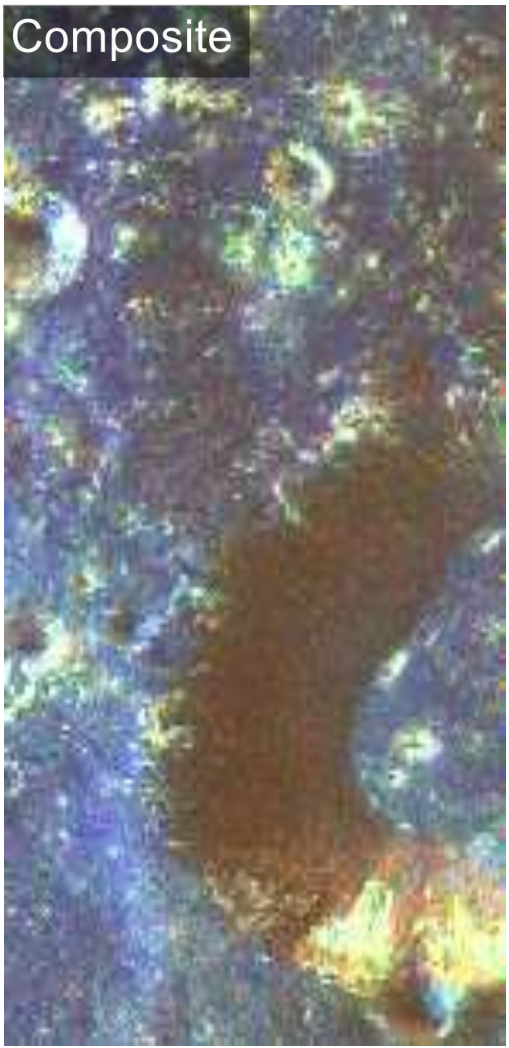

Figure 14